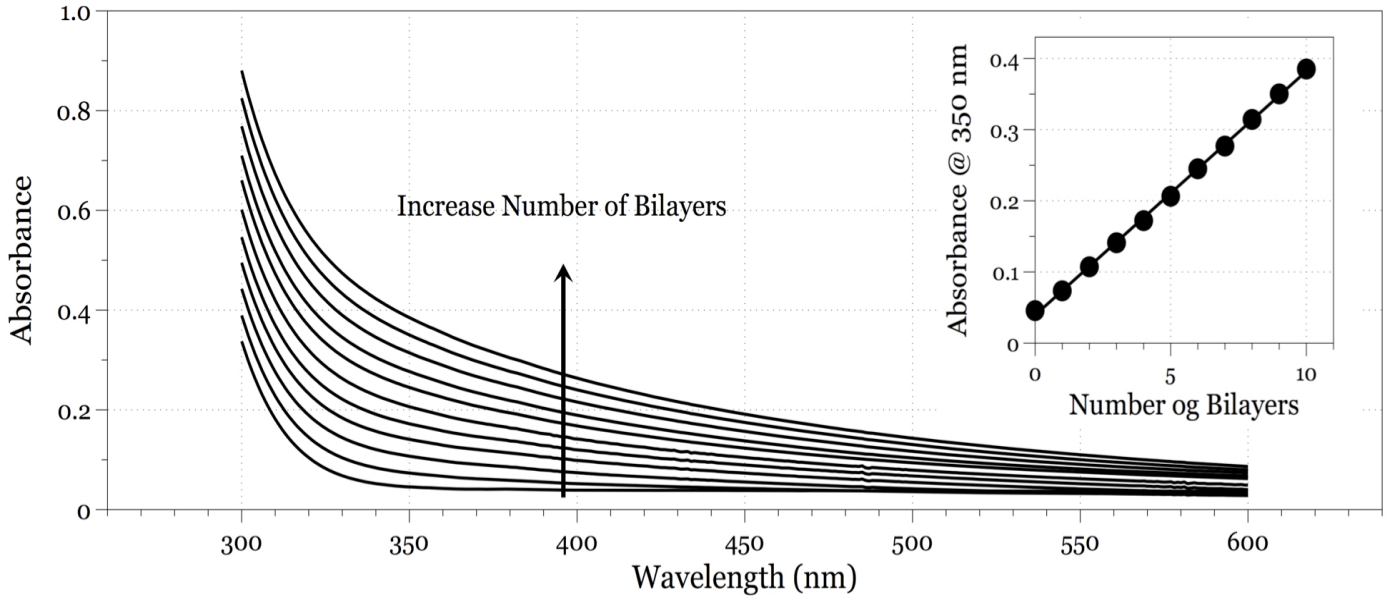

Figure 3.2 UV-Visible spectroscopy of PDDA/zeolite-L membrane deposition. The growth is perfectly linear to the number of layers deposited, indicating precise thickness control by LBL assembly.

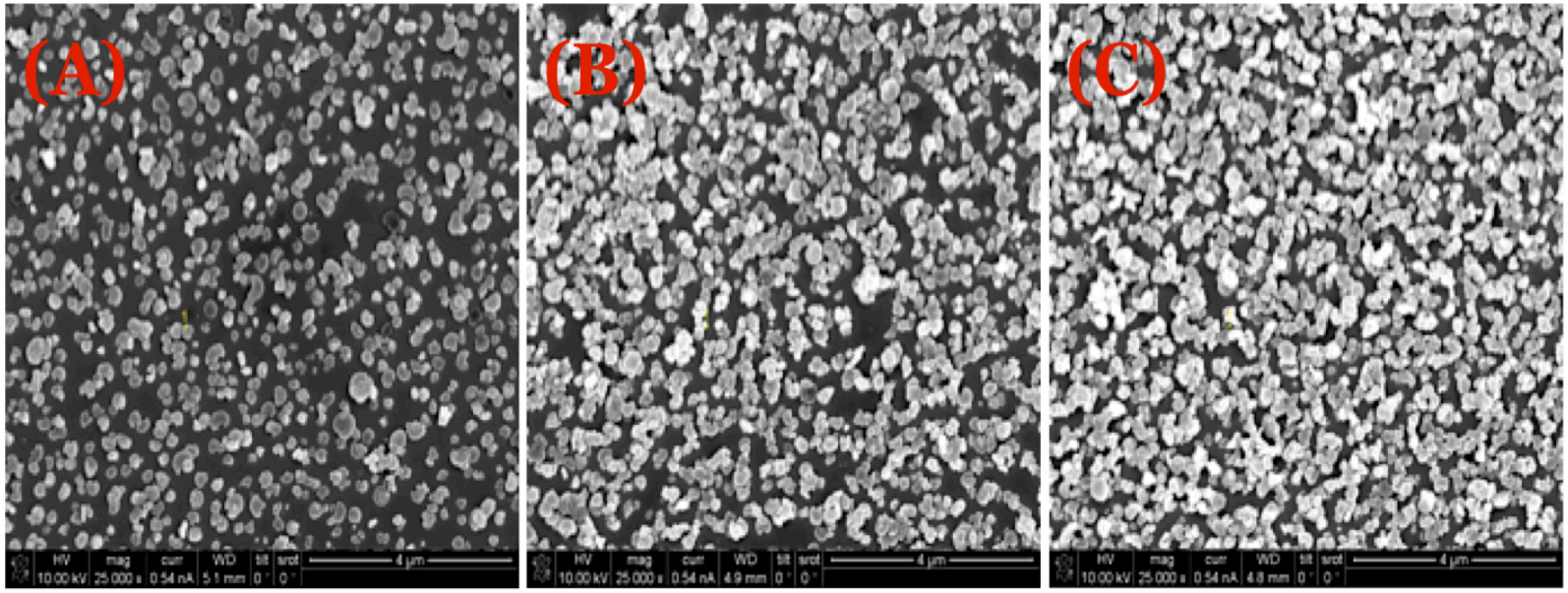

Figure 3.3 SEM image of 1-3 bilayer s of PDDA/zeolite deposited on silicon substrate. Disk-shaped zeolite-L nanocrystals are sitting flat on top of each other with well aligned c-axis.

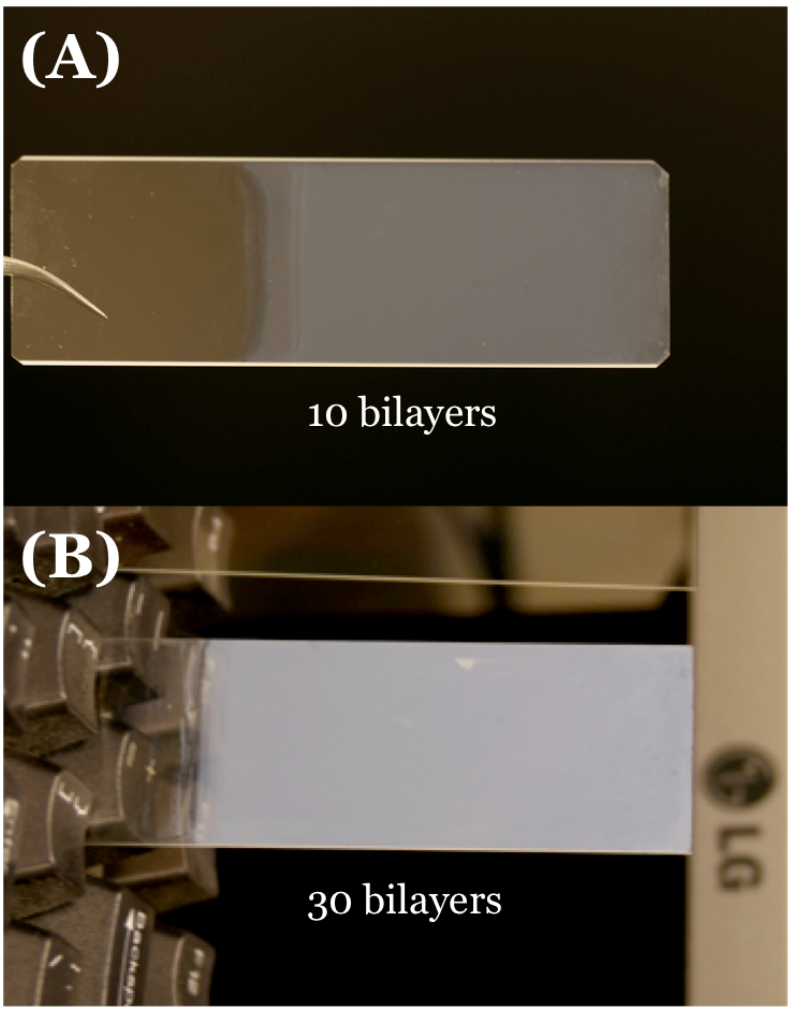

Figure 3.4 10 bilayers (A) and 30 bilayers (B) of PDDA/zeolite-L coating on clean glass slides. The thin films are very uniform and homogeneous, suggesting steady deposition and growth rate during LBL process.

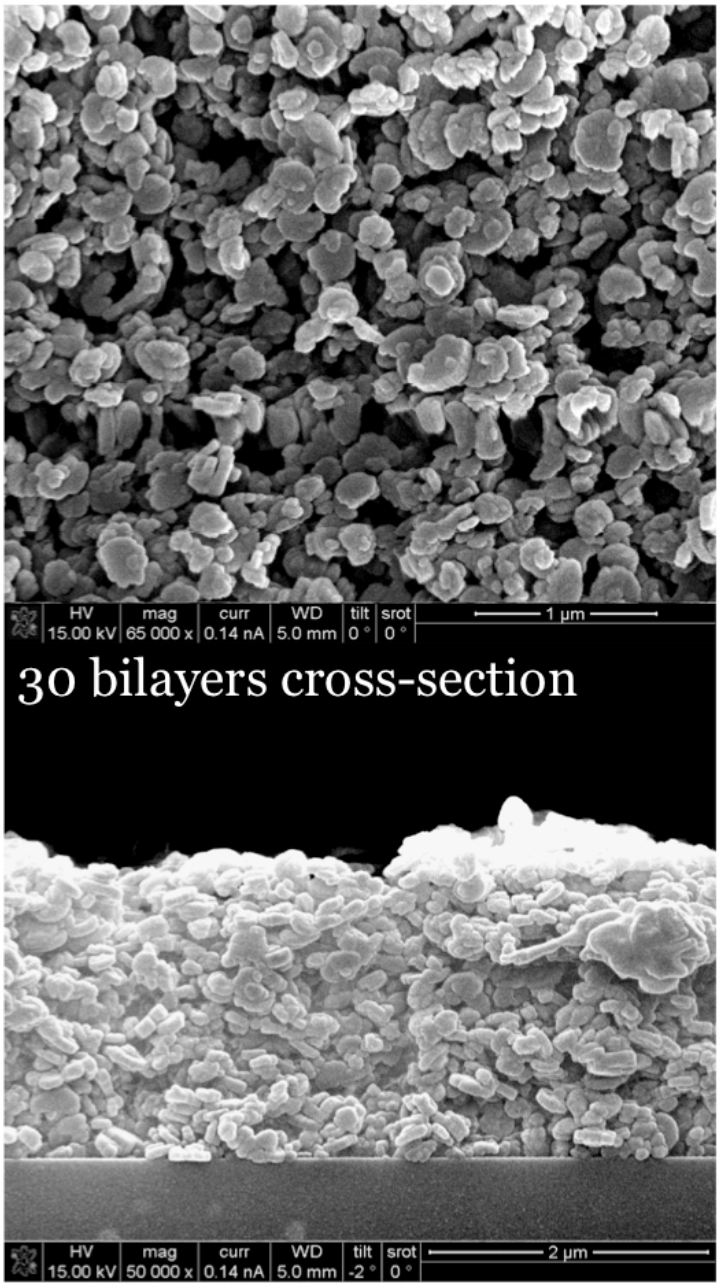

Figure 3.5 Picture and high-resolution SEM images of 30-bilayer PDDA/zeolite-L membrane. Top-view (top) and cross-section (bottom) show well-aligned zeolite nanocrystals. Note that the vertically deposited zeolite particles in the cross-section image are due to the cutting and breaking of the sample for imaging purpose.

3.4 Zeolite-L Modified Electrodes

3.4.1 Effects of PDDA/Zeolite-L Coating

Different numbers of Zeolite-L nanocrystals are deposited on conducting ITO electrodes (NANOCS, 50 Ω/sq) and cyclic voltammetry is performed to characterize the electrochemical response of zeolite-modified electrodes. 10 μM of potassium ferrocyanide ($K_3Fe(CN)_6$, Sigma) in 0.1M KCl (Sigma) solution is used as redox indicator and electrolyte based on well-established literature. The reason for low ferrocyanide concentration is to test the sensibility of ZMEs. Potentiostat (Epsilon) is used with Ag/AgCl as reference electrode. ZMEs with 1 cm^2 surface area are immersed in the electrolyte as working electrode and platinum mesh (1 cm^2) is used as counter electrode. Voltammograms are recorded for analysis and comparison after 100 cycles. A bare ITO electrode is always tested before each ZME is tested as reference.

First PDDA/zeolite-L modified electrodes were tested using cyclic voltammetry technique with different scan rate. 12 bilayers of PDDA/zeolite-L were deposited on ITO electrode to form the ZME. With increase scan rate, the $[PDDA/zeolite\text{-}L]_{12}$ electrode showed linear increase in response, suggesting good charge transfer with in the LBL framework (Figure 3.6). Second, $[PDDA/zeolite\text{-}L]_{12}$ electrode was compared to ITO bare electrode without any modification to see the redox reaction enhancement effect. In Figure 3.7, at scan rate of 50 mV/s, one can find $[PDDA/zeolite\text{-}L]_{12}$ LBL modified electrode, represented by the solid line, has mush higher peak current density than the ITO bare electrode, which is denoted by the dotted line. This experiment primarily

suggested that even with the thick and homogeneous coating of zeolite-L nanocrystals on the surface of the electrode, the diffusion of the redox species and charge transfer in the system not only remained intact, but even promoted.

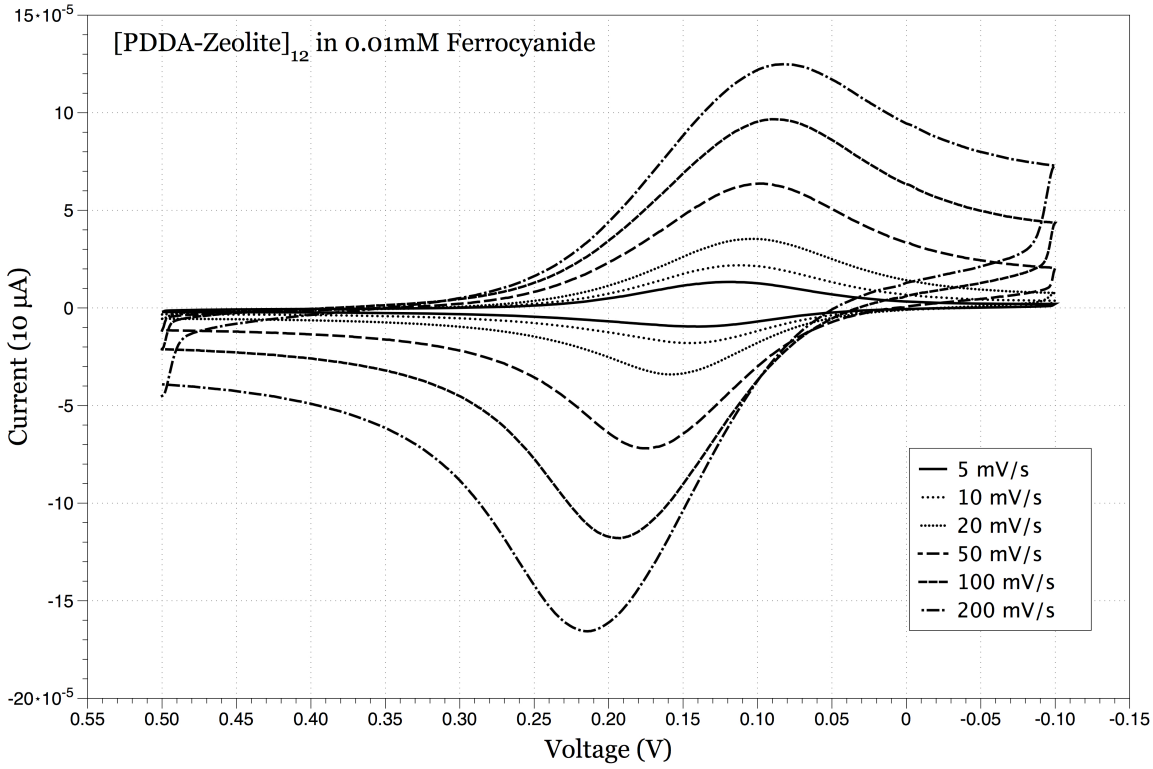

Figure 3.6 Cyclic voltammograms of $[PDDA\text{-}Zeolite]_{12}$ under different scan rate.

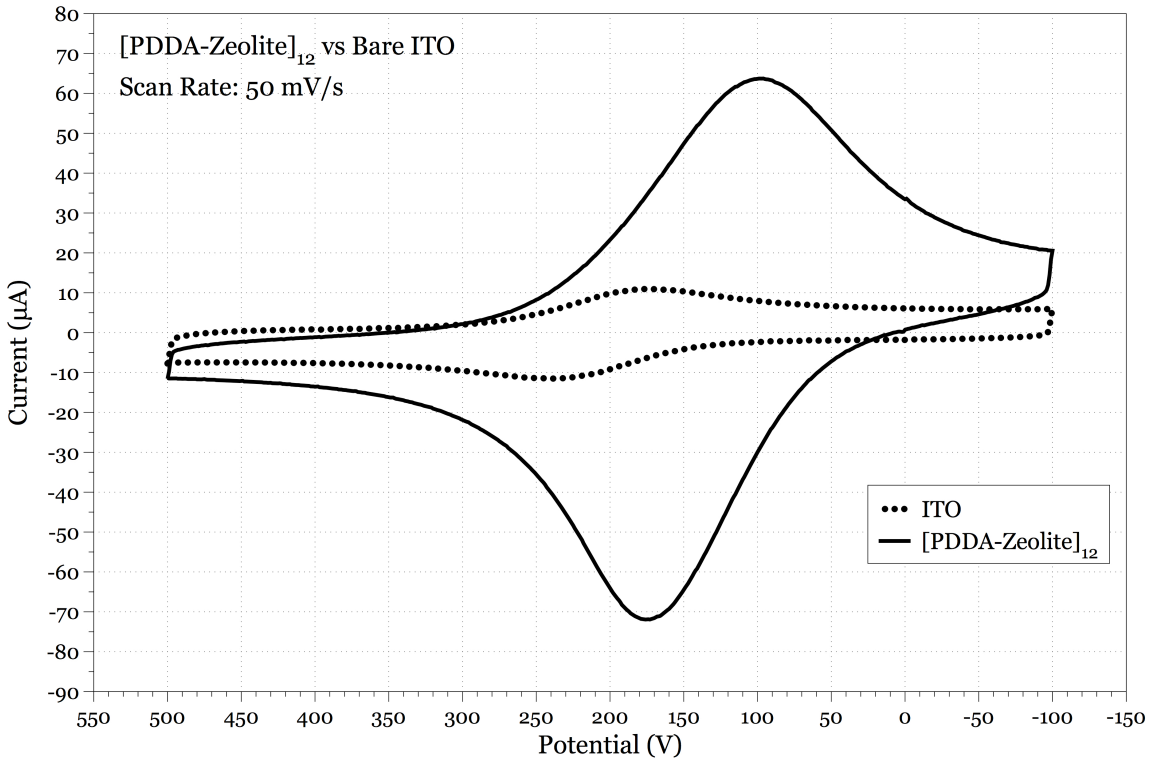

Figure 3.7 Signal enhancement by PDDA-zeolite coating during Ferrocyanide redox reaction, compared to bare ITO electrode.

3.4.2 Effects of the Unidirectional Channels inside Zeolite-L

Although it's a known fact that some zeolite species can be used as concentrators in industrial applications, to confirm the signal enhancement effect originates not from the porous structures but from special ionic conducting channels within zeolite-L framework, PDDA/zeolite-L single bilayer on ITO electrode (Figure 3.8(B)) was compared to anode aluminum oxide (AAO) on platinum electrode (Figure 3.8(A))[144]. Both cyclic voltammograms were taken with $K_3Fe(CN)_6$ as redox indicator. In the case of porous AAO on platinum electrode, significant redox peak suppression can be found due to the blocking effect of Al_2O_3 no matter how porous the material was. In PDDA/zeolite-L case, although 50% of the ITO electrode surface was covered by nanocrystals, redox peaks remained the same or higher compared to ITO bare electrode suggesting ferrocyanide molecules still had full or even better access to the electrode surface. These two experiments concluded that the enhanced diffusion or charge transfer originated from the special channel structures inside zeolite-L nanocrystals.

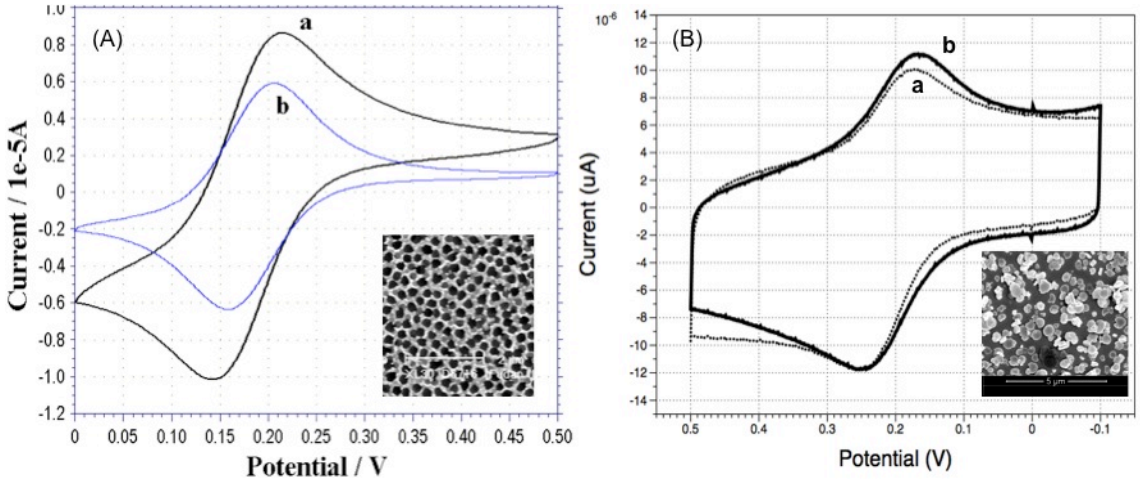

Figure 3.8 (A) Cyclic voltammogram of porous anode aluminum oxide (AAO) on platinum electrode (b) and platinum bare electrode (a) in $K_3Fe(CN)_6/Na_2SO4$ solution (b) ; (B) CV (scan rate: 50 mV/s) of PDDA/zeolite-L single bilayer on ITO electrode (b) and ITO bare electrode (a) in $K_3Fe(CN)_6/KCl$ solution. In AAO case the transport rate as well as redox reaction are suppressed by the AAO deposition, while in PDDA/zeolite-L case, no redox signal was reduced, indicating intact transport and electron exchange.

3.4.3 Effects of PDDA/Zeolite-L Coating Thickness

When different number of bilayers of PDDA/zeolite-L are deposited onto ITO electrodes, significant enhancement of redox reaction difference based on the thickness of the coating can be clearly observed (Figure 3.9). With the same scan rate, thick deposition layers do NOT reduce electron exchange between ferrocyanide and ITO electrode despite the fact that both PDDA and zeolite themselves are electrically insulating species. Based on cross-section SEM images, number of bilayers was converted to actual thickness of the PDDA-zeolite thin film deposited. In Figure 3.10, one can find the relationship between the thickness of PDDA-zeolite coating on ITO electrode surface and peak current density of Ferrocyanide redox reaction. The thicker the coating is, the higher the peak current density gets, and the better the enhancement. A very interesting enhancement plateau around 13-14 μm of PDDA-zeolite coating thickness can be found, which suggested the saturation of redox species near the vicinity of reaction sites. At this point, the concentration of the redox species in the bulk solution became the limiting factor that held back the diffusion and charge transfer.

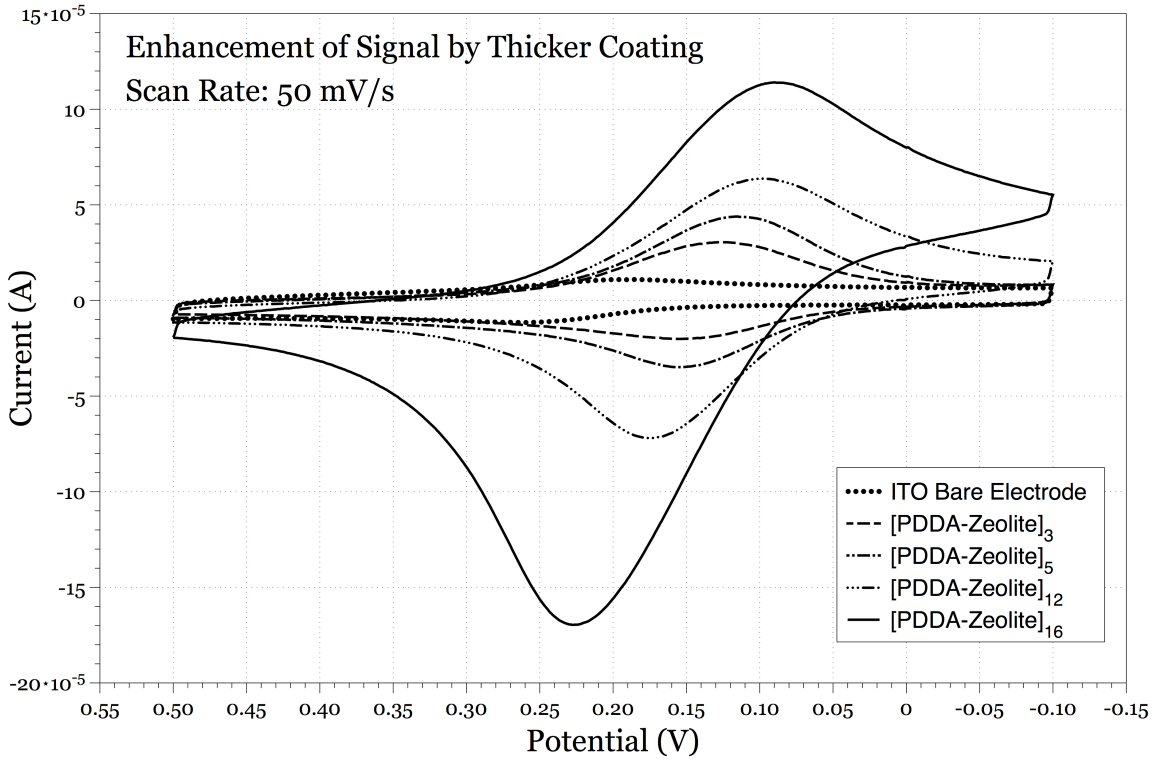

Figure 3.9 Significant redox peak enhancement observed in ZMEs with thicker PDDA/zeolite-L deposition

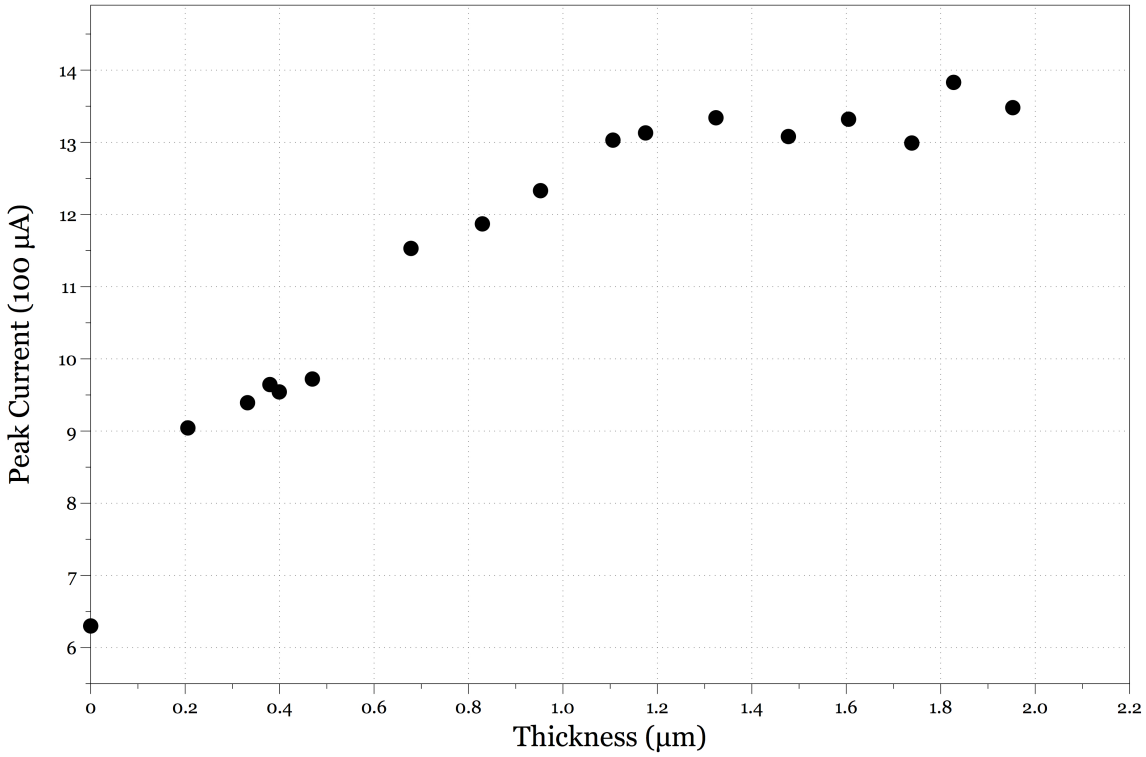

Figure 3.10 Relationship between the thickness of PDDA-zeolite coating on ITO electrode surface and peak current density of Ferrocyanide redox reaction. The thicker the coating, the higher the peak current density. Enhancement reaches a plateau around 13-14 μm of PDDA-zeolite coating.

3.4.4 Transport Behavior in PDDA/Zeolite-L LBL Membranes

Three possible mechanisms might contribute to the enhancement of redox signal: 1. Ferrocyanide molecules can freely diffuse through the channels inside zeolite-L nanocrystals and get oxidized/reduced at the ITO electrode surface; 2. Adsorption of ferrocyanide molecules inside zeolite-L channels makes the ferrocyanide concentration in the vicinity of the electrode surface higher than bulk; 3. Active ionic/electron transport makes all zeolite channel surface active for redox reaction. Figure 3.11 illustrates zeolite-L channels and the ferrocyanide molecule structures. The channel size in zeolite-L is calculated to be about 0.71 nm in diameter, while the size of ferrocyanide molecule is determined to be 0.62 nm. This suggests that the diffusion of ferrocyanide molecules in and out of the channels and through the channels is fairly slow, and rules out mechanism number 1.

For an electroactive species near in the vicinity of electrode, the magnitude of the current is described by the equation:

$$I_t = nFAD_0(\frac{\partial C}{\partial X})_x \qquad \text{(Eq. 3-1)}$$

where I_t is the current at time t, n is the number of electron transferred, F is the Faraday's constant, A is the electrode area, D_0 is the diffusion coefficient of the species, X is the distance from the electrode surface, and finally C is the concentration of the electroactive species. If the enhancement of the redox current is not from the improved diffusion of species in the channels, the observed higher redox peak must result from some other factors, such as higher concentration gradient near the electrode surface or higher surface area for reaction. Higher concentration is normally the outcome of high adsorption of

molecules, and to confirm the adsorption of ferrocyanide in zeolite-L channels, for the comparison, 10 bilayers of PDDA/PSS (poly(styrene sulfonate), Sigma) are deposited on ITO electrode to reach comparable thickness with PDDA/zeolite-L single bilayer. Cyclic voltammetry is then performed. In Figure 3.12 one can find significant signal suppression when PDDA-PSS was deposited on ITO electrode. Compared to the peak current density from PDDA/Zeolite-L in Figure 3.7, nearly two orders of difference between the signals from PDDA-Zeolite-L and PDDA-PSS can be observed. The results show that polymer thin films can only block and reduce electrode surface area. No redox peak enhancement and hence no adsorption of ferrocyanide molecules in the PDDA/PSS LBL film is observed.

Therefore we can hypothesize that ferrocyanide molecules are adsorbed inside the zeolite-L channels rather in polymer phase, and making the concentration of the redox species much higher near the electrode surface. The more deposited zeolite-L nanocrystals, the more adsorbed ferrocyanide species inside the PDDA/zeolite-L composite framework, and hence the higher the redox peak intensity until bulk concentration became the limiting factor. After each CV measurement, every ZME was rinsed under 18 MΩ DI water (de-ionized water) for 5 minutes, followed by immersion in clean DI water for 5 minutes, and finally another rinse under DI water for 5 minutes. Then the ZMEs were tested again in CV again in 0.1M KCl without redox species to investigate desorption of ferrocyanide molecules. No redox peaks could be found after cleaning processes described above, suggesting thorough desorption of ferrocyanide from

PDDA/zeolite-L matrix, and that the physiosorption of the redox species in zeolite-L framework is a fully reversible process.

Furthermore, there is also a possibility that active ionic/electron transport makes all zeolite channel surface active for redox reaction. Li *et al* proposed intrazeolite electron transport mechanism in electroactive species-zeolite system in 1995[145]. There are three possible mechanisms at zeolite-modified electrodes: (a) intrazeolite ion transport mechanism, (b) intrazeolite electron transfer mechanism, and (c) extrazeolite mechanism. In the first mechanism, the electroactive species are reduced after diffusion from the solution through bulk zeolite to the interface, and then the reduced species diffuse from the interface back to the bulk zeolite, as shown in Figure 3.13(a). This mechanism doesn't apply to our system as we already ruled out the possibility of high diffusion rate of ferrocyanide in zeolite-L channels because of their small size difference. In the extrazeolite mechanism (Figure 3.13(c)), the electroactive ions are first ion-exchanged by electrolyte cations into the solution in an extrazeolite process, and then diffuse to the substrate electrode where they are reduced. This mechanism does not apply to our system either, because potassium chloride is used as supporting electrolyte and does not involve in the redox reaction. The last mechanism, the intrazeolite electron transfer mechanism, illustrated in Figure 3.13(b), fits our system very well. In this mechanism, the electroactive species are reduced at the sites where they are located within the zeolite. This demands sufficient electron/hole conductivity mainly through the channels of the zeolite.

A simple capacitance measurement was performed to investigate this mechanism. ITO bare electrode, single, and ten bilayers of PDDA/zeolite-L on ITO were immersed in 0.1M KCl with 50 mV/s scan rate without any redox species (Figure 3.14). The results showed that the capacitance of the ZME goes higher when more zeolite-L nanocrystals were deposited on the electrode surface. The increase of active surface area inside zeolite-L must come from active electron or hole transport inside the channels. This supports the hypothesis of intrazeolite electron/hole transport mechanism that high electron/hole conductivity to the sites where electroactive species are located is established on the channel wall inside zeolite-L. The channels in zeolite-L nanocrystals are parallel, through the crystal, and aligned to *c*-axis, this is very different from other types of zeolite particles.

Early in 1988, Shaw *et al* conducted a systematic study on the voltammetric response of zeolite-modified electrodes using A and Y type of zeolite with electroactive ferrocyanide[146], and none of mentioned zeolite types gave current enhancement. In Table 3.1, one can find that the enhancement factor of zeolite-A and Y in ferrocyanide redox reaction was 0.12 and 0.31, respectively. Compare our findings with Shaw's, one can easily see that the main difference lies in channel configuration. Within the three kinds of zeolite particles, namely zeolite-A, zeolite-Y, and zeolite-L, only zeolite-L has straight-through-the-crystal channels. Without the straight channels, zeolite-A and zeolite-Y both suppressed the redox current pairing with ferrocyanide. As shown earlier in Figure 3.3 and 3.5, layer-by-layer assembly puts disk-shaped zeolite-L nanocrystals on top of each other with pretty aligned orientation. This contributes to the active and continuous

transport of either electroactive species or electron/hole in the channels. Layer-by-layer assembly coupled with zeolite-L is indeed an advantageous system for zeolite-modified electrodes.

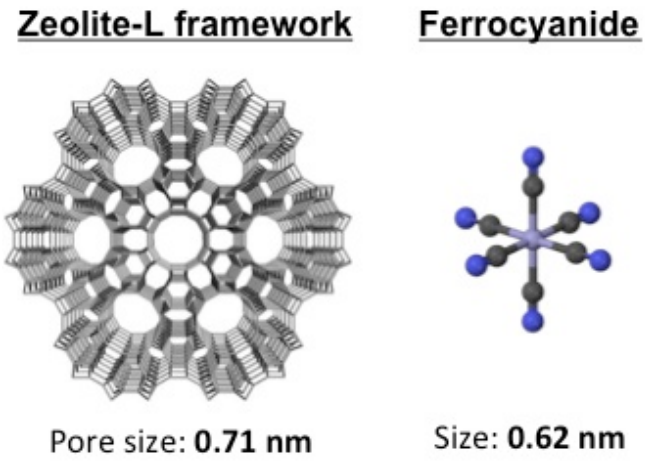

Figure 3.11 Zeolite-L nanocrystals have channels aligned with c-axis with size about 0.71 nm. 0.62 nm of ferrocyanide molecules can freely diffuse in and out the zeolite-L framework and get oxidized/reduced at the electrode surface.

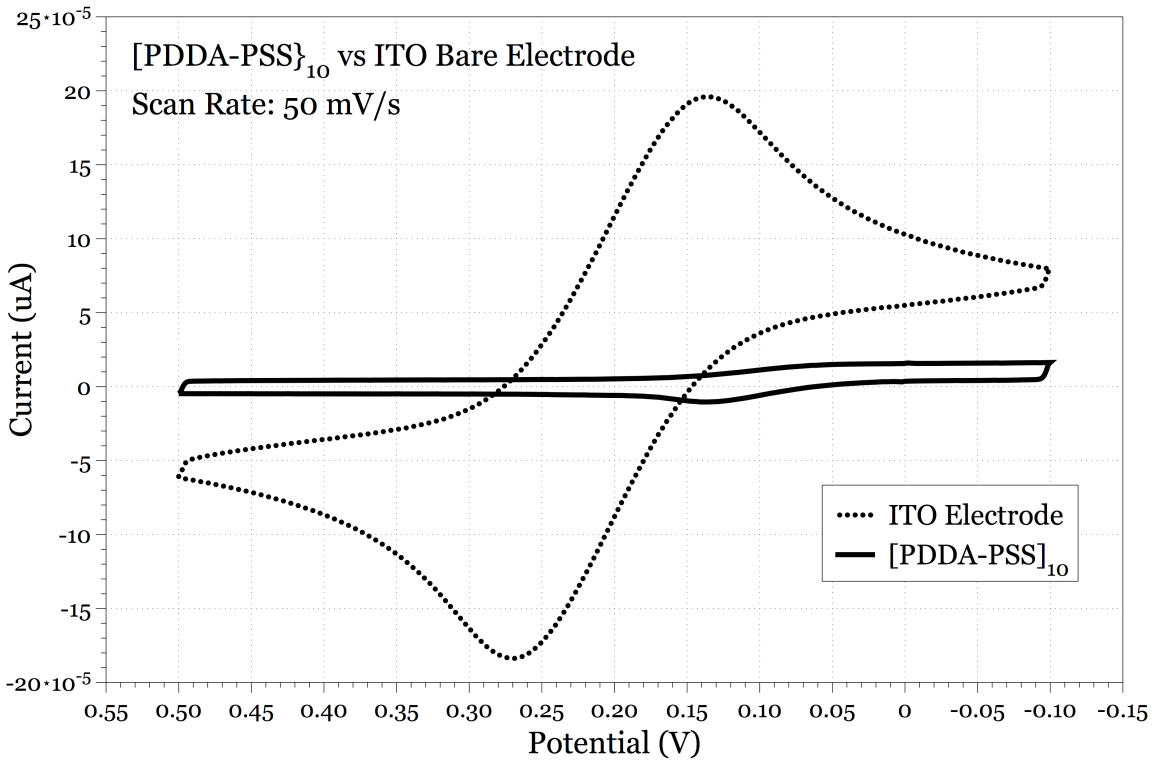

Figure 3.12 Signal suppresion by PDDA-PSS coating during Ferrocyanide redox reaction, compared to bare ITO electrode.

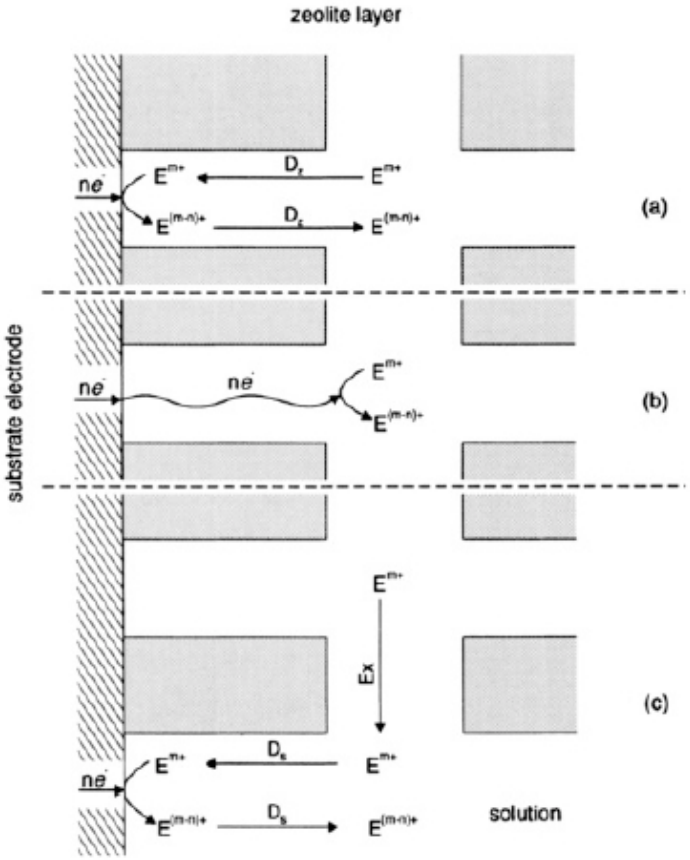

Figure 3.13 Three possible mechanisms at zeolite-modified electrodes: (a) intrazeolite ion transport mechanism, (b) intrazeolite electron transfer mechanism, and (c) extrazeolite mechanism. D_z and D_s represent the diffusion of ions within the zeolite and in solution, respectively. Ex indicates ion exchange at the zeolite/solution interface. The diffusion of cocations within the zeolite and ion exchange of electrolyte cations at the zeolite/solution interface are not indicated.

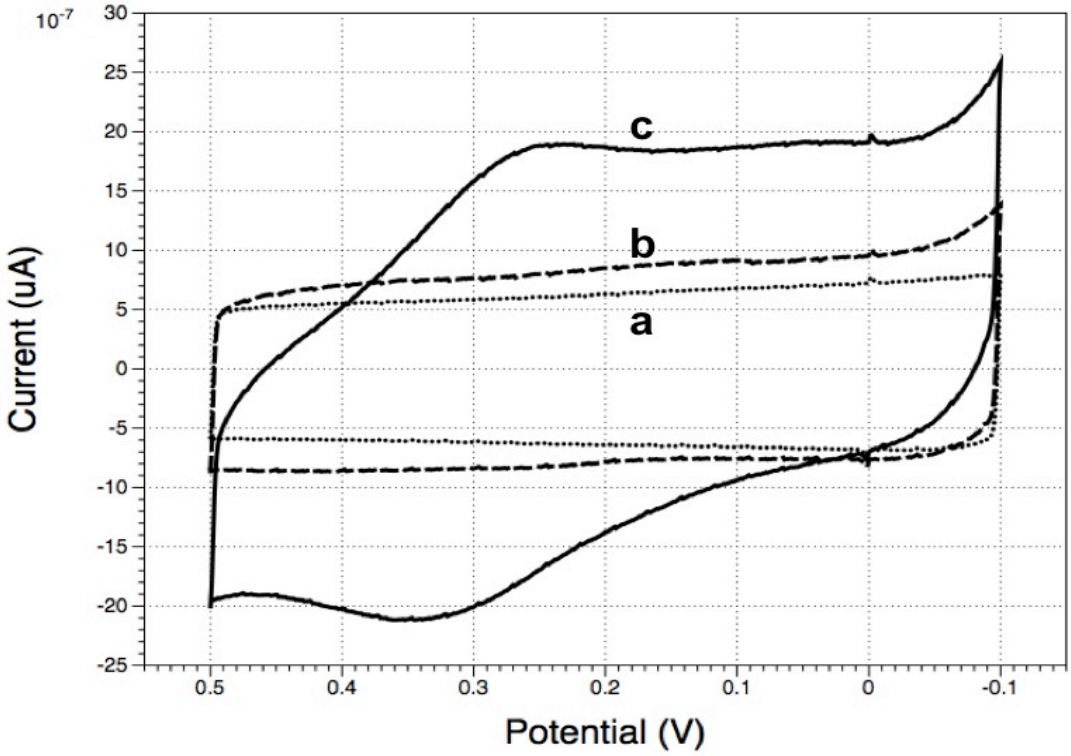

Figure 3.14 Capacitance measurement of ITO bare electrode (a), single PDDA/zeolite-L bilayer on ITO (b), and 10 bilayers of PDDA/zeolite-L on ITO (c). Higher capacitance comes from thicker PDDA/zeolite-L deposition, which indicates higher electrode surface area and higher charge capacity. Scan rate 50 mV/s in 0.1M KCl.

Electrochemistry of probe	$E^{o\prime}$ (V *vs.* SCE)	Ability of probe to enter zeolite[a]		Enhancement factor[b]	
		A	Y	A	Y
$MV^{2+} + e^- \rightleftharpoons MV^{+\cdot}$	−0.688[d]	−	+	0.69[f]	—
$MV^{+\cdot} + e^- \rightleftharpoons MV^{o}$	−1.12[d]			1.23[g]	6.93[g] (42.50)[h]
				0.98[g]	2.81[g]
$PV^{2+} + e^- \rightleftharpoons PV^{+\cdot}$		−	−	0.99	1.00
$PV^{+\cdot} + e^- \rightleftharpoons PV^{o}$					
$HV^{2+} + e^- \rightleftharpoons HV^{+\cdot}$	−0.600[d]	−	−	0.87	0.89
$HV^{+\cdot} + e^- \rightleftharpoons HV^{o}$	−0.800[d]				
$Ru(NH_3)_6^{3+} + e^- \rightleftharpoons Ru(NH_3$	−0.032[e]	−	+	<< 1	1.5 (68.3)[i]
					1.4 (5.8)[j]
$Fe(CN)_6^{3-} + e^- \rightleftharpoons Fe(CN)_6^{4-}$	+0.120[e]	−	+	0.12	0.31
$Cu^{2+} + 2e^- \rightleftharpoons Cu^{o}$	+0.099[e]	+	+	0.16	3.2
				0.76 (Li^+)[k]	1.96 (Li^+)[k]
				1.6 (K^+)[k]	2.9 (K^+)[k]

Shaw *et al., J. of Electrochem Soc.*, Vol 135, No. 4, 869-876, **1988**

Table 3.1 Enhancement effects during different redox reactions with kind of zeolite species modified electrodes. Only suppression effects was found using Zeolite A and Y

3.5 Investigation of Similar Systems

Since zeolite is basically aluminosilicate framework, some similar nanocrystals were studied to compare with PDDA/zeolite-L system. Enhancement effects from PDDA-SiO_2 and PDDA-Clay coating on ITO substrate were studied using the same cyclic voltammetry setup (Figure 3.15). Silica is known to have charge carrier transfer phenomenon at nanoparticle/water interface[147]. PDDA-SiO_2 system showed very similar current enhancement effect as PDDA/zeolite-L system. However, even with comparable thickness, the enhancement factor was not as large as zeolite-L. Lack of channel structure, fewer adsorption sites, and not as active charge transport could be the reason why PDDA-SiO_2 system didn't perform as well. In PDDA-Clay system, one can observe easily that the oxidation peak vanished while the reduction peak showed very good signal enhancement, suggesting irreversible reaction on PDDA-Clay modified electrodes. The mechanism of redox reaction at clay-modified electrodes is not the main focus in this study, but it definitely worth more detailed investigation.

Lastly we demonstrate the fixation of molecules inside zeolite-L LBL membrane through ionic exchange. PDDA/zeolite-L membrane on ITO electrode is immersed in high concentration ferrocyanide solution (5M) overnight, followed by sufficient rinsing with 18 MΩ de-ionized water for 5 minutes. The membrane showed green color instead of white, indicating successful fixation of foreign molecules inside zeolite-L framework. Significant oxidation and reduction peaks can be found when cyclic voltammograms are taken in 0.1M KCl without redox species (Figure 3.16). A second redox peaks and third reduction peak when scanned at higher potential range could be found, which were

contributed by the redox reaction of the foreign molecules fixed in different "cage structures" inside the aluminosilicate framework[148]. Similar results were demonstrate by Zhao *et al* with zeolite-Y, but the redox peaks are not as significant as using zeolite-L as foreign molecule carrier.

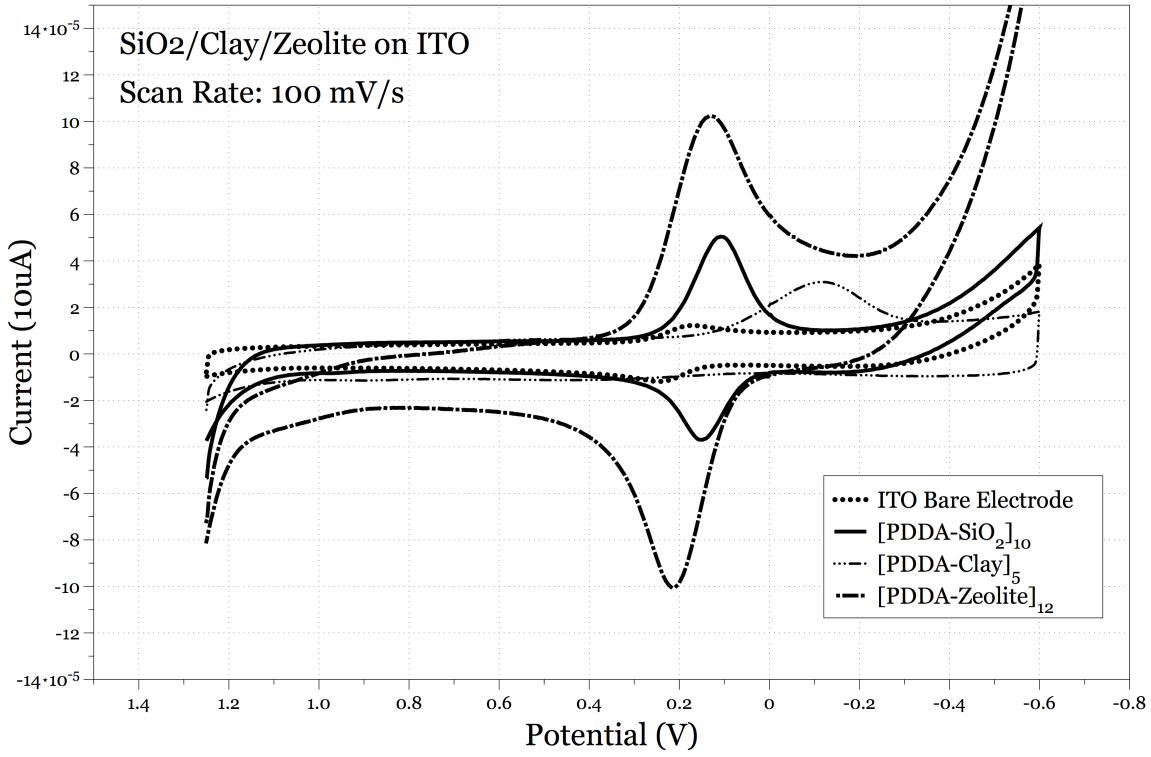

Figure 3.15 Enhancement effects from similar PDDA-SiO_2 and PDDA-Clay coating on ITO substrate. They both exhibit similar enhancement effects, however, not as dramatic as PDDA-zeolite coating. One can also observe the asymmetric redox peaks from PDDA-Clay suggesting irreversible reaction on PDDA-Clay modified electrodes.

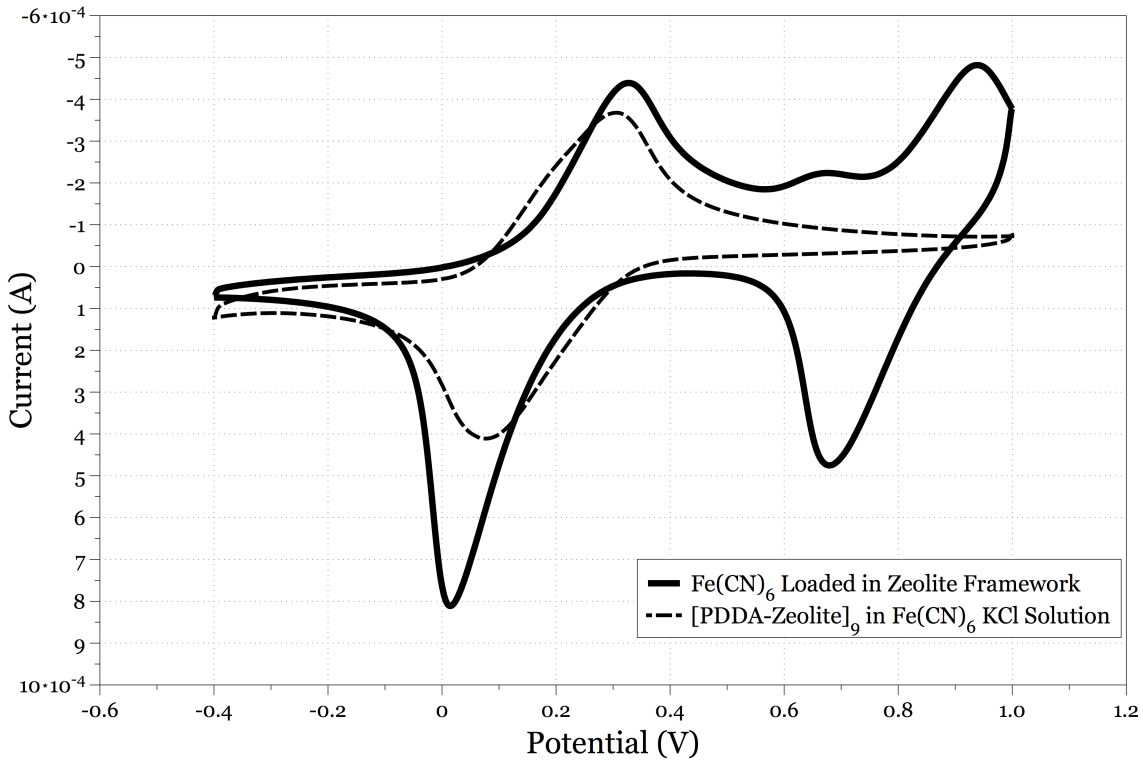

Figure 3.16 Cyclic voltammetry of ferrocyanide loaded zeolite-L membrane on ITO in 0.1M KCl (solid line) compared to ZME described earlier in 10 μM ferrocyanide + 0.1M KCl (dash line). Significant second redox peak pair and third reduction peak when scanned at higher potential range could be found, which were contributed by the redox reaction of the foreign molecules fixed in different "cage structures" inside the aluminosilicate framework

3.6 Conclusion

In this work we use layer-by-layer assembly technique to make polyelectrolyte PDDA and negatively charged zeolite-L nanocrystals into thick and uniform coating on ITO electrodes. SEM images show that most of the deposited disk-shaped zeolite-L nanocrystals are sitting flat on top of each other with the same orientation. Ionic conducting channels inside zeolite-L nanocrystals are hence aligned with c-axis, making the transport in the direction vertical to the electrode surface possible. Electrochemical characterization shows dramatic enhancement of redox peaks when zeolite-L modified electrodes are used, and the thicker the zeolite-L layer, the better the enhancement. By investigating the physiosorption behavior of redox species ferrocyanide in PDDA/zeolite-L LBL composite matrix, we confirm that although ferrocyanide cannot diffuse freely in and out the channel due to the larger size of the channels, the adsorption of ferrocyanide in the PDDA/zeolite-L membranes dramatically increases the concentration of the ferrocyanide molecules in the vicinity of the electrode surface. The active electron/hole conducting nature of zeolite-L nanocrystals also contributes to the increase of active redox surface area. Finally we successfully demonstrate the feasibility of loading PDDA/zeolite-L LBL matrix with foreign molecules, which can turn interesting zeolite-L modified electrodes into molecular probes.

Chapter 4

Ionic Conducting LBL Membranes for Lithium Batteries

4.1 Introduction

Solar and wind energy sites require high power, high discharge rate energy storage capabilities. Among several potential methods of accumulation of solar and wind energy, which typically include conversion to hydrogen[149, 150] and supercapacitors[151,] lithium ion batteries emerge as the most optimal option in respect to both cost and energy capacity[152-156]. Lithium batteries research started as early as 1970's, when Wittingham *et al.* proposed using intercalation lithium compound lithium titanium disulfide as high-energy-density cathode[157]. With metallic lithium as anode, the rechargeable battery had energy density of 0.48 kWh/kg. After nearly three decades of development, in 1991, Japanese company Sony revealed the first generation of commercial lithium batteries for consumer electronics. The high energy-to-weight ratio makes them the most common power supplies in portable electronics. Their low loss of charge over time and lack of memory effect also contribute to extended life cycles and popularity among mobile devices. In recent years, automobile industry, military, and even aerospace researches are also devoted in the battery research to improve energy density, durability, safety, and cost.

It has been shown that lithium ion batteries can also meet the performance demands required for the large-scale energy storage capabilities[158, 159]. Moreover, considering recent advanced in anode and cathode materials LIBs have a potential to effectively compete with supercapacitors in respect to discharge rates[160, 161]. Considering the cost of platinum in fuel cells and other factors, such as energy losses during chemical conversion steps, lithium batteries are considered now to be more advantageous and cost-effective solution than hydrogen gas[162-164]. Besides LIBs, lithium metal polymer batteries (LMPBs) should also be considered as an appropriate technological target for energy storage as well because of the improved discharge rates and importance in many other sectors of technology including automotive industry, which is intrinsically connected with reduction of carbon emissions and foreign oil dependence. However, otherwise promising LIB and LMPB technologies suffer from poor safety[165] and cycle performance. These issues can be traced in large part to the nucleation and growth of lithium dendrites[166] and the flammability of liquid or polymer ion-conducting media that separate the anode and cathode. Dendritic deposits[9] (Figure 4.1) in LIBs (formed as a side reaction) and LMPBs can penetrate quite easily through traditional ion-conducting membrane (ICM) separators and cause short-circuits during repeated charge-discharge cycling. Several approaches have been taken to reduce dendrite growth in electrolytic cells, but none can prevent it entirely without changing the nature of the ion-conducting separator[1, 167]. Transformational technologies are required to mitigate dendrite formation and substantially change the properties of ICMs. There are no materials currently available that would have the required mechanical properties, ionic conductivity, and electrochemical/thermal stability. New manufacturing approaches are inevitably needed

to achieve necessary mechanical strength, ionic conductivity, and safety in lithium batteries for large energy sites.

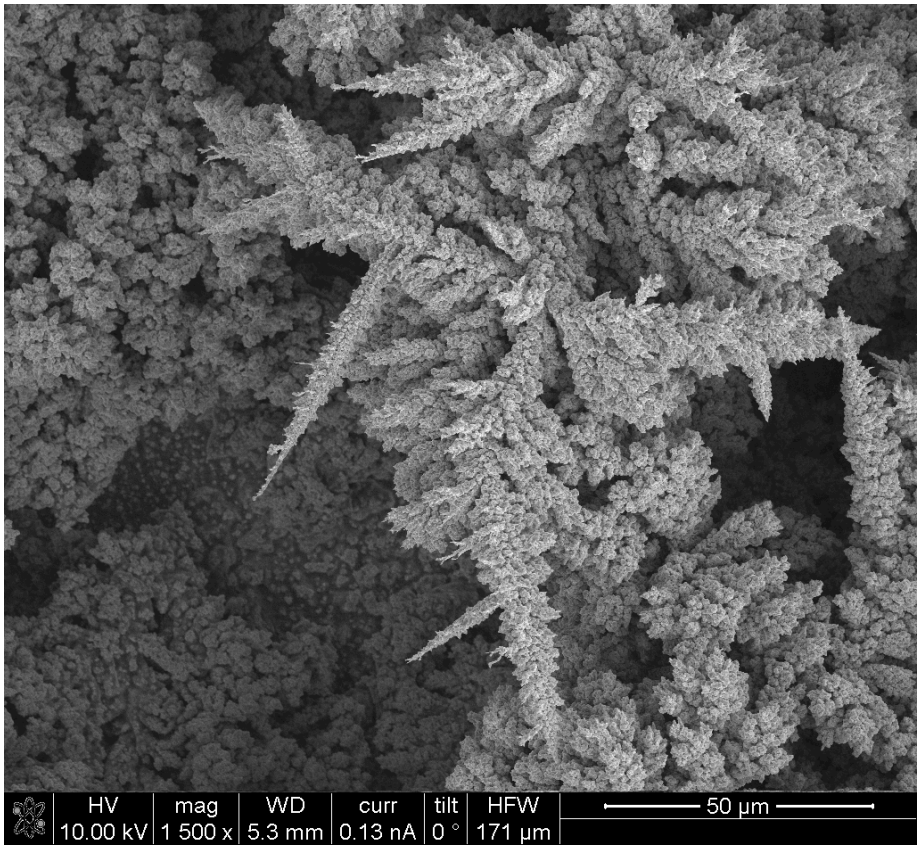

Figure 4.1 A dendritic deposit, produced on battery prototype during the repeated cycling of a battery unit. (Kotov Lab).

4.2 Challenges of Lithium Anode Batteries

Lithium is a logical choice for an anode material because its standard reduction potential (–3 V) and specific gravity (0.5) are the lowest of all metals. It was quantitatively confirmed as early as 1971 that these characteristics, along with lithium's low molecular weight, could be used to support widely variable discharge rates and provide extremely high energy density. Although not the first, the most widely cited early research on lithium-metal anodes was done by Exxon corporation[157], underscoring the importance of lithium-battery technology to the transportation industry. Shortly after this experimental program began, however, lithium-metal rechargeable batteries were proved impracticable. Dendritic deposits – so named because they look like trees or moss – formed on the metal during the charge cycle, inducing high explosion risk and suggesting the near inevitability of battery failure.

All types of lithium batteries are dogged by the risk of cell combustion or electrode degradation under high discharge rates. To circumvent these failure mechanisms, significant effort has been put toward the development of electrochemically inert, combustion-resistant separator materials. In lithium-ion batteries, polymer gels swollen with liquid electrolyte are typically employed as separator media[168]. This method stabilizes the battery system, but at the expense of power density, because the ionic conductivities of polymer gels are low compared to those of organic electrolytes[169]. As much as a quarter century ago, dry, solid-polymer electrolytes were also observed to inhibit failure mechanisms of lithium anodes[170], but only in systems operated with elevated temperatures to enhance ionic conductivity.

4.3 Lithium Dendrite Formation and Prevention Methods

In the last twenty years the dendrite problem has been circumvented by substituting metallic lithium for an insertion material, typically porous carbon[171, 172], at the expense of the minimal reduction potential of metallic lithium. The specific energy a battery delivers is proportional to the cell potential, so the use of carbonaceous anodes correlates directly to lower energy density. This deficiency is endemic to all commercial LIBs, which are distinguished from "lithium-metal" batteries by their graphitic anodes. Development of a robust dendrite-inhibition method would promise a quantum leap forward, allowing an energy-density increase of 30%[167].

Besides safety and durability issues caused by dendritic growth, lithium and lithium-ion batteries made by current technologies also have other problems: (1) Lack of strength and mechanical stability of current polymer electrolytes lead to poor contact at electrode-electrolyte interface and the instability of the battery performance. (2) Currently available solid-state electrolytes are fabricated mostly by casting methods, whereby ionic conducting polymer, lithium-ion conducting fillers, lithium salts, and solvents are blended together and allowed to dry to form thin membranes. This is a major downside because there is virtually no control either over the structure of the casted membrane or the placement of the filler. Fillers can form aggregates, the polymer can be re-crystallized, and lithium salts can be poorly distributed. All of these processes severely reduce ICM performance. (3) Flexibility is one key requirement for modern ICMs as "roll-up" geometry is widely proposed to enhance volumetric power density. Current electrolytes either lack adequate flexibility or mechanical strength required for several

important purposes. (4) It is a common practice to let the polymer or solid electrolytes adsorb lithium-ion containing liquids in order to promote transport. However, without proper control over the casting process, it is virtually impossible to independently optimize porosity, pore size, permeability, and wettability of the electrolytes.

Investigation by our group of dendrite growth through porous polymer separator is shown in Figure 4.2. Polished copper plates were used as electrodes to sandwich a piece of Celgard separator. 0.15 M of copper sulfate in 0.5 M of sulfuric acid was used as electrolyte, and was pre-loaded into Celgard membrane. A potential was supplied to the assembly to start copper deposition, which is a good simulation to battery charging process when lithium ions are forced to migrate from cathode to anode under a charging potential. Note that the deposition current is limited by the diffusion of copper ions, not the potential supplied. If we make a plot with supplied potential as x-axis, and deposition current density as y-axis, one can find the plateau forming from 350 mV to around 750 mV, where the current is dominated by diffusion of ions (Figure 4.3)[173]. Above 800 mV hydrogen evolution takes place and current density just shoots up. By controlling the concentration of ions in the electrolyte solution, we have the control over deposition current density, if supplied potential sits right in the plateau range. In our investigation, 700 mV of electrical potential was supplied to the copper-separator-copper assembly. We let it run as long as required until the circuit is shorted, indicating the dendrites have grown from one electrode to another. In a typical run, the time it takes to short the circuit is about 15 minutes, when the deposition current density is at around 50 mA/cm^2. SEM images (Figure 4.4) show the dendrite growth through Celgard 2400 membrane after just

a short period of charging current. Now consider these metallic dendrites growing in battery cells and eventually short the circuits. Although lithium metal anodes are not commonly implemented in lithium batteries yet due to safety issues, dendrite growth is inevitable in most type of lithium battery cells, it's just a matter of time before metallic passages are created to shutdown the cells.

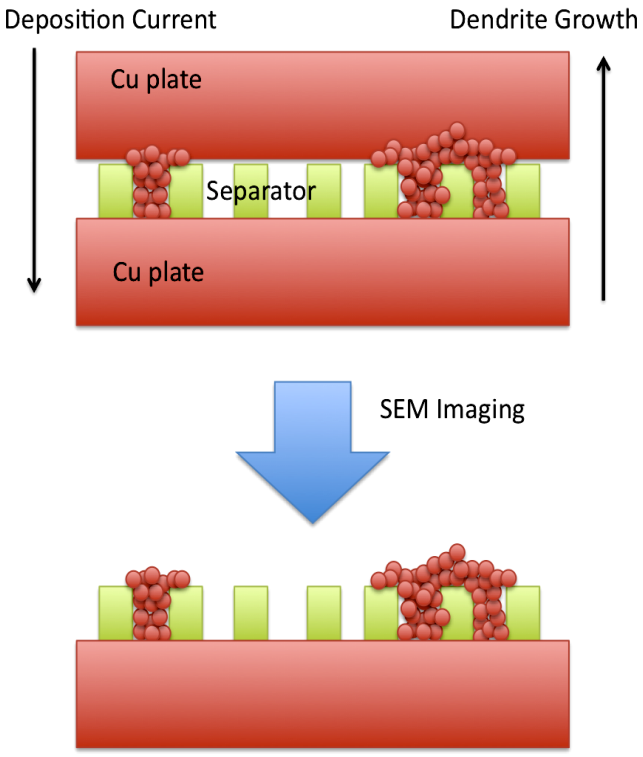

Figure 4.2 Illustration of dendrite growth setup through commercial porous polymer separator. Copper was used instead of lithium for the ease of investigation in room temperature and atmosphere.

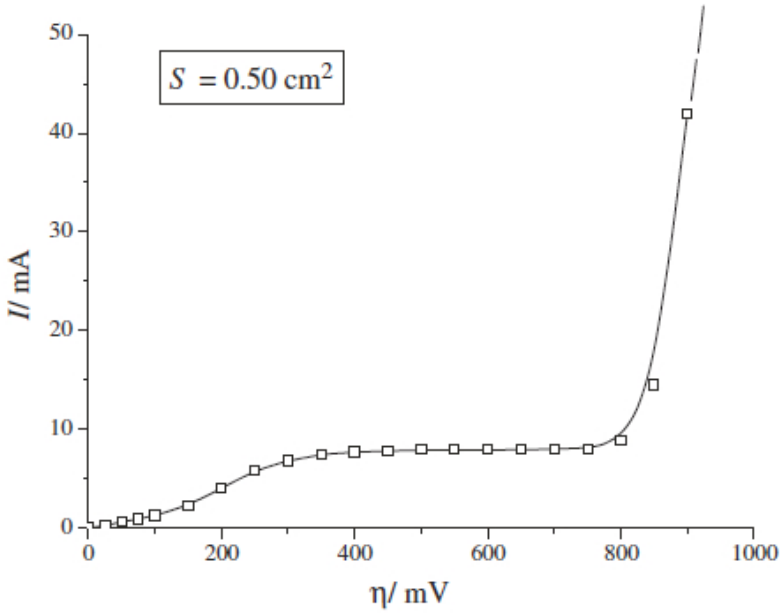

Figure 4.3 Polarization curve for the cathodic process of copper deposition from 0.15 M $CuSO_4$ in 0.50 M H_2SO_4 (Nikolic *et al*, 2006)

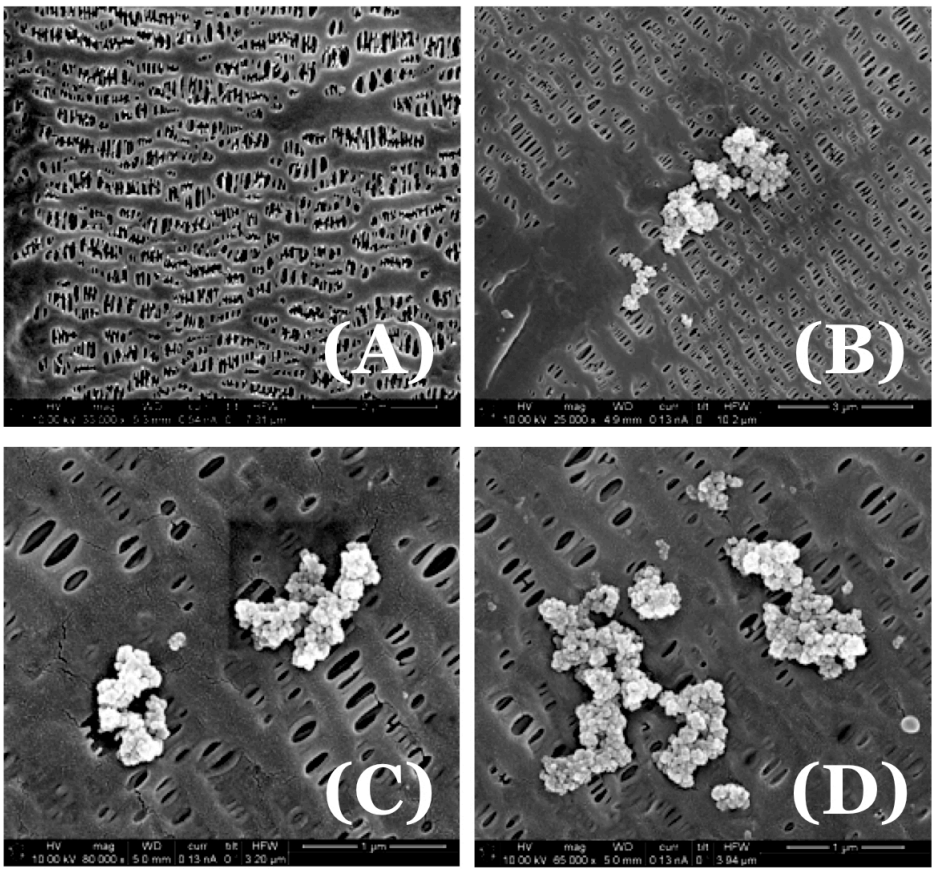

Figure 4.4 Through-the-separator copper dendrite growth under SEM. (A) Celgard 2400 separator before dendrite growth; (B, C, D) Copper dendrites deposited through the pores of the separator

Several approaches have been taken to eliminate dendrite formation in electrolytic cells, including the incorporation of additives to improve plating morphology or create inert solvent/solute mixtures and use of novel anions. For instance, 0.5 g/L addition of saccharin was used to form dendrite-free nanorystalline Ni-Cu alloy coatings with mirror-finish surfaces1. Hybrid-gel electrolytes combine high conductivity of liquid electrolytes with the mechanical strength of solid polymer electrolytes have also shown to delay dendrite growth[6]. Researchers have used the hydrogen bubbles generated during electrodeposition to change the growth morphology of ramified zinc[7]. Also, magnetic fields have been utilized to manipulate the morphology of dendrites during the electrodeposition of copper[8]. Polymer-based electrolytes are also known to inhibit dendrite formation due to the mechanical strength of the separator; however, these systems underperform due to the high operating temperatures (up to 90°C) required to obtain desired conductivity for good battery performance[167].

A new class of solid-state ionic materials generally known as "superionic solids" obtained by ion intercalation has attracted interest as alternatives to conventional ionic conducting liquid electrolytes. It has been demonstrated that, in principle, material with high stiffness may also support high ionic conductivity if molecular structure is properly designed. Solid electrolytes have the advantages that they may block propagation of dendrites. However, to lead to transformational changes in battery technologies solid state electrolyte materials also require the following properties[171], which they currently do not have: (1) Ionic conductivity higher than 10^{-4} S/cm at room temperature to achieve a performance level close to that of the liquid electrolyte-based devices; (2) Cation

transference number as close as possible to 1 to ensure maximum number of potential transporting ions are moving in the polymer electrolyte; (3) High chemical, thermal and electrical stabilities; (4) High mechanical toughness and flexibility, so the scale up to large-scale manufacturing of the devices (especially in the rolled-up batteries) can be realized; and (5) Compatibility with highly oxidizing or reducing electrode materials.

Lately several glass-based solid electrolytes with high Li^+ conductivity have been developed such as ceramic lithium solid electrolyte [xLi_2O-BPO_4][174] lithium-ion-conducting ceramic $Li_{13}Al_{0.3}Ti_{17}(PO_4)_3$ and polyethemrethane/lithium triflate polymer electrolyte. Test results showed that a siginificant conductivity increase could be achieved by exposure of the ceramic to gaseous DMF, acetonitrile, or water. Different techniques like mechanical milling have been employed to develop more homogeneous, efficient Li^+ ceramic electrolytes that exhibit high charge-discharge voltage ratings (4.5 V vs. Li/Li^+)[175] with high membrane stability under water, without sacrificing ionic conductivity. Li_2S-based oxysulfide glasses and sulfide glass-ceramics enhance Li^+ conductivity via a "mixed-anion effect," achieved by combining sulfide and oxide anions, and precipitation of superionic metastable crystals by careful heat-treatment of glasses. In fact, Li^+ conducting solid electrolytes with the highest conductivity and the lowest activation energy for conduction have been achieved in the Li_2S-P_2S_5 glass-ceramics with ionic conductivity as high as 3.2×10^{-3} S cm^{-1} at room temperature. Conductivity of Li_4-xGe_1-xP_xS_4 can also be maintained values as high as 10^{-3} S cm^{-1}[1176], likely owing to the formation of superionic metastable phases upon heating.

4.4 Lithium-Ion Conducting Electrolyte Membranes

4.4.1 Lithium Battery Electrolytes

Electrolyte is one of the crucial components in a battery cell. It acts like a carrier for lithium ions between anode and cathode to complete the circuit loop inside the battery when the battery passes an electric current through external circuits. When battery cells undergo discharging state, lithium ions move from negative to positive electrode through electrolyte until the potential between two electrodes is in equilibrium, while in charging state, lithium ions move back to negative electrode from positive one and the electrical potential between the two electrodes is restored. A good electrolyte needs to provide high ionic conductivity to promote lithium ion transport. High stability under high voltage and temperature is also a key feature to a good electrolyte.

Liquid electrolytes for lithium batteries are commonly implemented and advantageous owing to their high transport and high ionic conductivity in comparison to other categories of electrolytes. Since the voltage provided inside lithium battery cell are higher than the potential at which aqueous electrolytes can electrolyze, generally liquid electrolytes are made by adding lithium salts, such as $LiPF_6$, $LiClO_4$, $LiCF_3SO_3$, and LiTFSI, into organic solvents, such as acetonitrile, ethylene carbonate, propylene carbonate, and dimethyl carbonate. Typically the ionic conductivities of liquid electrolyte at room temperature (20°C) are in the range of 0.01 S/cm, increasing by 30-40 % at 40°C, and decreasing when temperature goes lower. The advantages of liquid electrolytes, like those containing lithium hexafluorophosphate, lithium sulfonates, or lithium

sulfonimides, are attributed to their high transport rates and consequently hence high ionic conductivity. However, their disadvantages include corrosion of electrodes, limited range of operating temperature, electrolyte leakage, flammability, and metal dendrite nucleation at the electrode interfaces during multiple charge-discharge cycles. Dendrite formation is a particularly important failure mechanism, particularly for LMPBs. Dendrites may propagate during the charge cycle, when metal deposits grow away from the electrode and into the bulk electrolytic solution[10], forming bush-like or needle-like structures that can internally short circuit a battery. Dendrite growth occurs at currents near the limiting current[177], and therefore limits battery charging rates.

Transport properties of electrolytic separators are key determinants of battery performance. In polymer electrolytes, efficiency can be lost due to ohmic drops, which arise from low ionic conductivity, diffusion overpotentials, caused by poor electrolyte transference, or mass-transfer limitations, represented by low salt diffusion coefficients. The latter two properties are most significant during high-rate charge and discharge, where suboptimal values limit power density of the battery. Ionic conductivity tends to be seen as the most important separator property because it correlates to both the heat generation and power efficiency of the battery at large[178]. In principle the ICM should have as high a loading of lithium ions as possible, to ensure high conductivity. Typical ICM materials are observed, however, to pass through conductivity maximum at around 1 M electrolyte loading. In this range, contrary to popular belief, ion pairing and ion-ion interactions may dominate over chain motion in determining transport characteristics[179]. It is crucial that a separator model account for ion-ion interactions as well as ion-polymer

interactions. From a phenomenological point of view, this requirement means that diffusion coefficient, transference number, and ionic conductivity must be included as independent properties, and that thermodynamic characteristics describing polymer/salt interactions should also be known[180]. Moreover, since the charging and discharging of a battery induce concentration gradients in the separator, a suitable model should account for the observed strong composition dependence of transport and thermodynamic properties[181].

4.4.2 Importance of Membrane Mechanical Properties

The physical purpose of an ICM is to provide an electrically insulating, ionically conductive transport medium with very high mobility of the active species. A number of practical concerns, however, actually overshadow this function in implementations of lithium batteries. From a chemical perspective, ICMs for lithium-ion batteries must be noncombustible, to ensure consumer safety[165]; they must degrade very slowly outside of their thermodynamic stability range, in order to tolerate the high potentials typical of modern cathode materials[182]; and they must facilitate the formation of a protective layer on the anode surface, to prevent irreversible side reactions[167]. Each of these subsidiary functions of an ICM can be served fairly well by poly(ethylene oxide), or PEO. PEO also facilitates the dissociation, and consequent rapid transport, of electrochemically stable lithium salts (such as lithium perfluorosulfonimides). But even after all of these physical and chemical needs are met, rechargeable LIBs are still subject to the nucleation and growth of dendrites during the charge cycle.

An ICM's ability to inhibit dendrite formation hinges on its mechanical properties. Experimentally, nanocomposite PEO-based polymer materials, which exhibit enhanced viscosity and/or elasticity, have been observed to afford not only high conductivity and active-species mobility, but also to enhance stability of the lithium-metal surface during charging[183]. Dendrites form on electrodes during metal reduction because protrusions from the electrode surface are exposed to a higher potential and ionic concentration than recesses. This fact induces protrusions to amplify over time. The major factors that inhibit dendrite growth are mechanical resistance/robustness of ICM

and surface tension. The original literature on electrochemical dendrite formation comes from the field of electroplating, where electrolytes tend to be aqueous. In these systems electrolyte viscosity is relatively low and surface tension provides the dominant force resisting dendrite growth. Numerous theoretical studies, including one by a member of our team, have shown that the mechanical properties of liquid electrolytes are insufficient to ensure morphological stability during electrodeposition[184]. Importantly, dendrite propagation has been shown experimentally to conform with the predictions of these models[185].

While studies of stagnant liquid electrolytes are overwhelmingly negative with regard to lithium-electrode stability, the research into lithium dendrite inhibition by solid, high-modulus solid-polymer electrolytes has been encouraging. Mechanical properties of polymer electrolytes can be enhanced without sacrificing ionic conductivity, either by creating block copolymers[186] or nanocomposite materials[187]. In the former case, improved mechanical characteristics have been exploited to develop commercial lithium-metal batteries that can survive a thousand cycles without dendrites, with 50% higher energy density and one eighth the capacity fade of state-of-the-art lithium-ion batteries. Monroe's research has rationalized these observations from a theoretical point of view, using an analysis that accounts for how the deforming interface changes the kinetics of lithium deposition[184]. Combined with a linear stability analysis of the deposition kinetics, the research has shown that dendrite growth can be inhibited entirely by an ICM with double the shear modulus of lithium – about 7 GPa[12]. It is therefore imperative to move the theoretical analysis to the next step, and study how the physical, chemical, and

mechanical factors determining electrode stability interact during cycling of lithium-metal batteries.

4.4.3 Novel Nanocomposites for Lithium Batteries

In recent years, nanocomposites of ionic conducting polymers with inorganic/metal nanoparticles (NPs) as electrolyte materials for lithium batteries have drawn considerable attention as ideal materials for achieving high conductivity, power density, mechanical strengths, and design flexibility. Mechanistically, fast ion conduction at the highly conductive interface layer between the ionic conducting polymer PEO matrix and embedded NPs is possible owing to the large surface area of NPs and the highly polar functional groups on the surface such as –COOH and –OH[188]. Also, NPs prevent reorganization of polymer chains at room temperature. The incorporation of the NP filler can also reduce the crystallization of the polymer host and act as 'solid plasticizer' capable of enhancing the transport properties[189]. Furthermore, the NPs can react with anions and polymer segments to reduce ion aggregation, increase the fraction of free Li^+, and enhance ionic conductivity[190]. Electrolytes incorporated with metal NPs are known to exhibit higher Li+ transference number (~0.5) in contrast to pure polymer matrices (0.2~0.3). The mechanical stability and strength of the nanocomposite electrolytes are also improved by the incorporation of NPs. Nanocomposites already developed for lithium battery electrolytes can generally be categorized into 2 major groups: polyethyleneoxide (PEO)-based and polyvinylidenefluoride-co-hexafluoropropylene (PVdF-HFP)-based. PVdF-HFP is a fluorinated co-polymer that forms a porous medium and cooperates with lithium salts to deliver ionic conductivity as high as 1.2×10^{-3} S cm^{-1}. Clay[191], TiO_2, MgO, ZnO[5], SiO_2[192], and Sb_2O_3[193] NPs were demonstrated to improve the ionic conducting performance of PVdF-HFP-lithium-salt

system, for example, 5 wt% of Sb_2O_3 NPs produced ionic conductivity of the nanocomposite polymer electrolyte up to $2.98x10^{-3}$ S cm^{-1} at room temperature.

One of the most extensively studied polyether system is PEO due to its relatively low melting point and T_g, its ability to play host to a variety of lithium salts and different concentration ranges, and ability to serve as a binder for other phases[194]. Several investigations have shown that incorporation of NPs such as TiO_2[194-198], Al_2O_3[196, 199], SiO_2[200-202], hectorite[202], saponite[203], clay[204], chitin[205], cellulose whiskers[206, 207], polyether-grafted SnO_2[198, 208], and polyether-grafted ZnO[209] into PEO system can effectively improve ionic conductivity by few orders of magnitude even at high temperatures. Although overall performance of PEO-based nanocomposites doesn't show much difference from PVdF-HFP-based materials, it's very interesting that the transference number in PEO-based system is generally higher than other electrolytes. The transference number of PEO-saponite system and PEO-hectorite system approached near unity[202]. Other reports indicate PEO-TiO_2 of 0.6, PEO-SnO_2 of 0.57, PEO-SiO_2 of 0.56, and PEO-ZnO of 0.55. Therefore, these results clearly show that incorporation of NPs results in more current being carried across the nanocomposite electrolytes, which is a fundamentally desired feature of all battery cells.

4.5 ICMs from PEO-Kevlar LBL Nanocomposites

Here we present a new generation of ionic conducting nanocomposite membranes, made by layer-by-layer assembly of ionic conducting PEO and robust fibrous polymer Kevlar, that exhibit superior mechanical strength, good conductivity, and high flexibility that will make the progress a step toward better lithium metal batteries. Kevlar is the most robust and commonly used fibrous polymer material available so far. The high strength of Kevlar makes it popular for high performance armors, ropes and cables. Kevlar derives part of its high strength from inter-molecular hydrogen bonds formed between the carbonyl groups and protons on neighboring polymer chains and the partial pi stacking of the benzenoid aromatic stacking interactions between stacked strands. These interactions have greater influence on Kevlar than the van der Waals interactions and chain length that typically influence the properties of other synthetic polymers and fibers. PEO (polyethylene oxide) has adequate hydrogen bonding sites along the polymer chains, which can be perfectly utilized in the assembly of ultrastrong PEO-Kevlar nanocomposites. While crystallization of polymer can degrade performance, in PEO-based separator fabricated using layer-by-layer assembly with Kevlar as counter polymer, the re-crystallization of PEO phase can be inhibited and the performance of the cell will not be jeopardized even when working under higher temperature.

4.5.1 Preparation of Kevlar Nanofibers and PEO Solution

So far there is no literature published for the preparation of Kevlar aqueous solution due to the insolubility of the fiber in water. Alternatively, the Kevlar DMSO solution is prepared by the deprotonation reaction of Kevlar fibers with a common base potassium hydroxide (KOH) to easily yield DMSO dissolvable Kevlar polyanions. In a typical preparation, 1 g of Kevlar fiber and 1.5 g KOH are added into 500 ml DMSO solution. Under magnetic stirring at room temperature, the color of the solution turns red gradually, and eventually reaches dark red, which is a good indication of thorough breakdown of hydrogen bondings between kevlar bundles. 0.2 wt% Kevlar-DMSO dark red solution can be obtained after a week of continuous stirring (Figure 4.5).

PEO aqueous solution is prepared by dissolving as-received polymer in deionized water with gentle stirring. 0.05 wt%, 0.1 wt%, 0.5 wt%, and 1 wt% PEO aqueous solution with PEO molecular weight of 100K, 1M, and 4M were prepared.

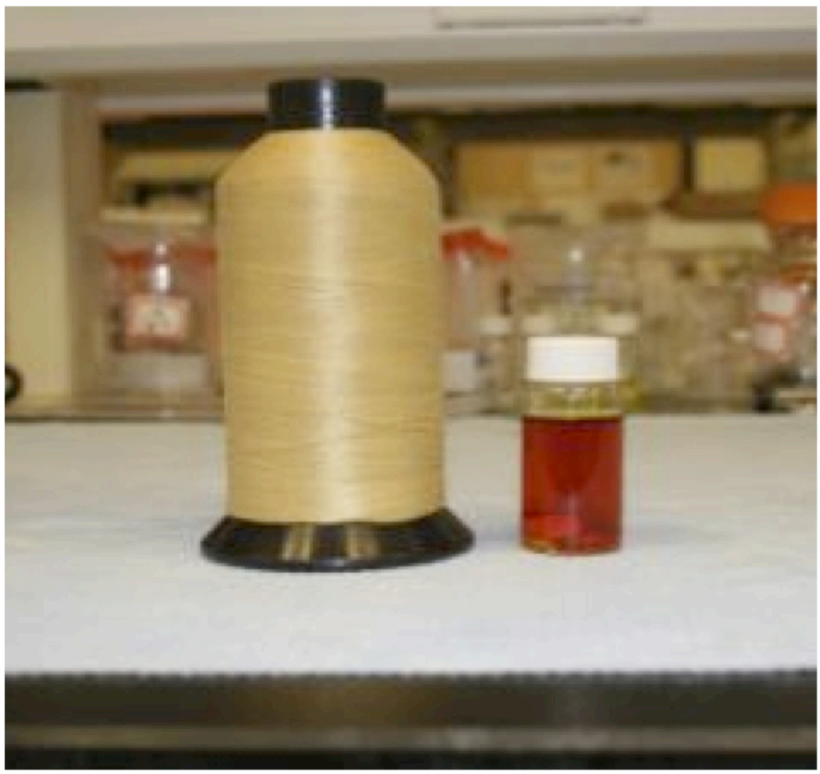

Figure 4.5 As-purchased Kevlar yarn and Kevlar-DMSO solution.

4.5.2 Layer-by-Layer Assembly of PEO-Kevlar Nanocomposites

Generally, layer-by-layer assembly deposited PEO-Kevlar membranes on glass slides by dipping in PEO solution and Kevlar-DMSO alternatively with rinsing steps in between each dipping process. Glass slides are pre-cleaned by piranha for 2 hours followed by sufficient rinsing in 18 MΩ DI water prior to the assembly. Dipping cycles are repeated many times until desired membrane thickness is reached. Intensive rinsing in DMSO for 30 seconds and 1 minute in DI water after Kevlar layer is implemented to promote homogeneity of the film. The moisture in the air and inside the film deposited on the glass slide can go into Kevlar-DMSO solution over time, making the dark-red color go lighter. The color of Kevlar-DMSO eventually becomes light yellow, at which point the chunks of Kevlar fibers are formed, and the solution is no longer good for LBL deposition. Normally Kevlar-DMSO solution is replaced with fresh one after 15-20 dipping cycles to ensure best thin film morphology and homogeneity.

The growth of a PEO-Kevlar LBL membrane on glass slides was monitored by UV-Visible spectroscopy every 2 bilayers up to 12 bilayers (Figure 4.6). By tracking the absorbance at 330 nm of wavelength, one can observe very steady and linear deposition rate of PEO and Kevlar nanofibers on glass slides (Figure 4.7). It also suggests homogeneous and exceptional adsorption of PEO and Kevlar polymers on the surface of glass slides. This is very typical build-up process by layer-by-layer assembly as well dispersed polyelectrolytes / nanomaterials are deposited on the substrate surface at nanometer scale. Figure 4.8(A) shows 100 bilayers of thick and homogeneous PEO-Kevlar membrane on glass slide. After deposition processes are done, PEO-Kevlar

membranes are detached from glass slides by immersing the slides in 0.1% HF and etching the glass underneath away. Freestanding membranes are rinsed several times with DI water and dried in vacuum oven. Image of a free-standing PEO-Kevlar membrane can be found in Figure 4.8(B). As shown in the picture, the membrane is translucent with light yellow to ivory color. The 100-bilayer PEO-Kevlar membrane is very easy to handle by tweezers, which is a good indication of high mechanical strength and stability. The shinny and nacre-like color of the surface under light suggests smooth and uniform surface morphology (Figure 4.8(B), inset).

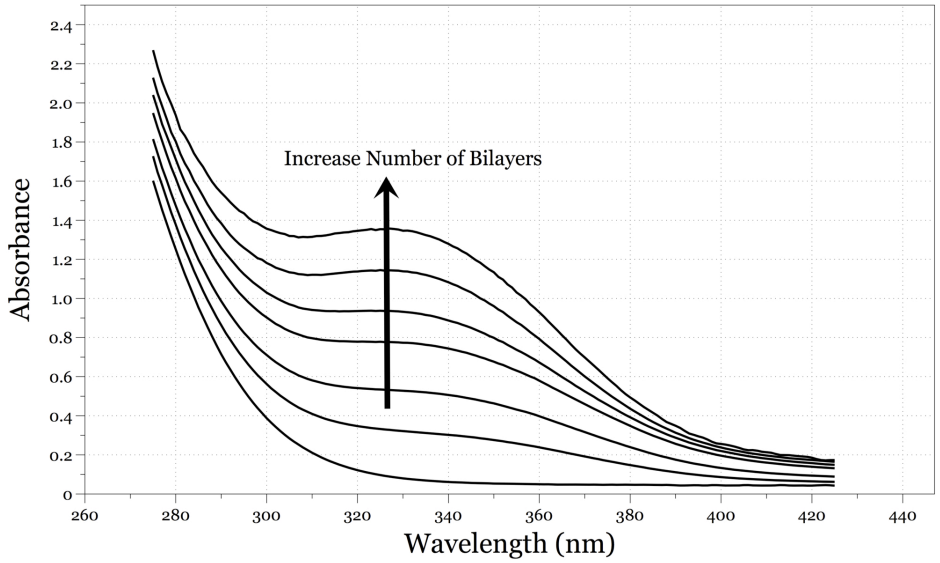

Figure 4.6 UV-Visible spectroscopy of PEO-Kevlar on glass slides.

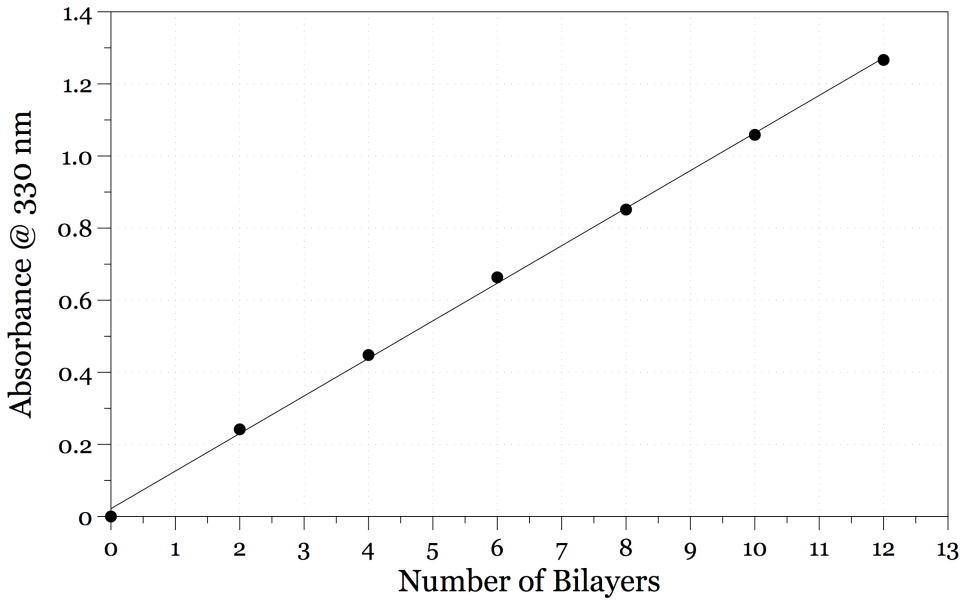

Figure 4.7 Linear growth tracked at 330 nm of wavelength of PEO-Kevlar on glass slides indicates uniform deposition and good membrane morphology.

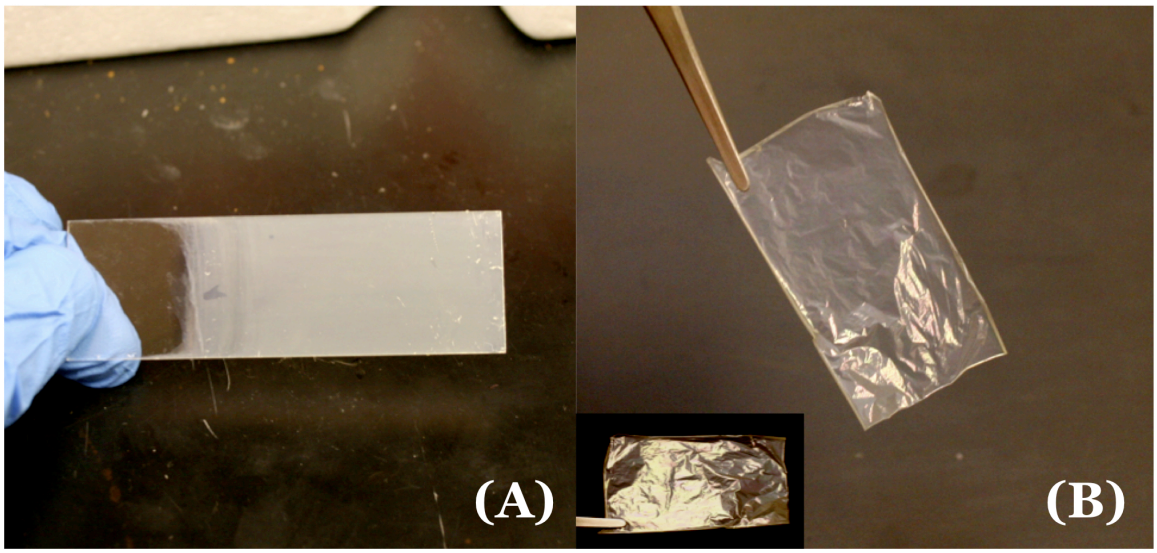

Figure 4.8 (A) Thick and uniform [PEO-Kevlar]$_{100}$ membrane on glass slide; (B) freestanding [PEO-Kevlar]$_{100}$

4.6 Characterization of PEO-Kevlar LBL ICMs

Transmission Electron Microscopy (TEM) was used to investigate the morphology of Kevlar nanofibers in DMSO solvent. Scanning electron microscopy (SEM) and atomic force microscopy (AFM) images were taken to study the morphology of the membranes as well as the thickness from the cross section. Ionic conductivity was obtained by sandwiching the membranes in between two 0.5-inch-diameter polished stainless steel electrodes and housed inside Swagelok Teflon PFA casings and analyzed by Solartron 1260 AC Impedance Analyzer. Ringku rotating anode x-ray diffractometer was used to investigate crystalline structures of PEO-Kevlar composite membranes. And finally, the mechanical properties, such as Young's modulus, ultimate strength, and thermal stability, were obtained and evaluated by mechanical tensile analyzer and thermal expansion analyzer.

4.6.1 Transmission Electron Microscopy

Joel 3011 Transmission Electron Microscopy was used to study Kevlar nanofibers. 20 μl of as-prepared Kevlar-DMSO solution was dropped on TEM grid. TEM images confirm that after 7 days of continuous stirring in basic environment, Kevlar nanofibers are mostly deprotonated, if not fully, and are well dispersed in DMSO solvent. Image of long Kevlar nanofibers can be found in Figure 4.9.

4.6.2 Atomic Force Microscopy

Nanoscope II Atomic Force Microscopy (AFM) was used to study surface deposition morphology of PEO-Kevlar. AFM images of PEO-Kevlar were taken after 5

bilayers of deposition on cleaned silicon wafer. PEO and Kevlar formed very dense and uniform interconnecting networks on the surface (Figure 4.10(A)). These network structures are the main structural support of the membrane. Not only does the stiffness of Kevlar nanofibers provide sufficient rigidity to the composite membranes, the interconnecting networks also provide passages that are capable of distributing external stresses uniformly across the whole regime, and prevent internal stress concentration that would easily crack thin films, which is very common and crucial for high-mechanical-strength materials. With Kevlar phase as mechanical reinforcement, PEO-Kevlar nanocomposite membrane electrolyte is expected to provide much higher mechanical modulus than common polymer electrolytes, such as pure PEO.

4.6.3 X-Ray Diffraction Spectroscopy

X-ray Diffraction Spectroscopy is a method of determining the arrangement of atoms within a crystal, in which a beam of X-rays strikes a crystal and diffracts into many specific directions. From the angles and intensities of these diffracted beams, a crystallographer can produce a three-dimensional picture of the density of electrons within the crystal. From this electron density, the mean positions of the atoms in the crystal can be determined, as well as their chemical bonds, their disorder and various other information. The XRD patterns of PEO-Kevlar nanocomposite membrane and pure PEO are shown in figure 4.10(B). The well defined crystalline peaks observed form pure PEO (Figure 4.10(B), inset) indicate a significant proportion of a crystalline phase compared to amorphous one. This is very common among polymeric materials that are made by casting and other similar methods. Crystalline structures are known to

dramatically decrease the ionic conductivity and hence the usability of PEO-based electrolyte. On the contrary, the x-ray diffraction pattern for PEO-Kevlar membrane made by layer-by-layer method shows no crystalline peaks at all. Through alternative deposition, the hydrogen bondings between PEO and Kevlar fix them in place, and greatly inhibit PEO polymer chains from re-crystallization. Therefore the ionic conductivity would not be jeopardized even when the membranes undergo abnormal thermal cycles.

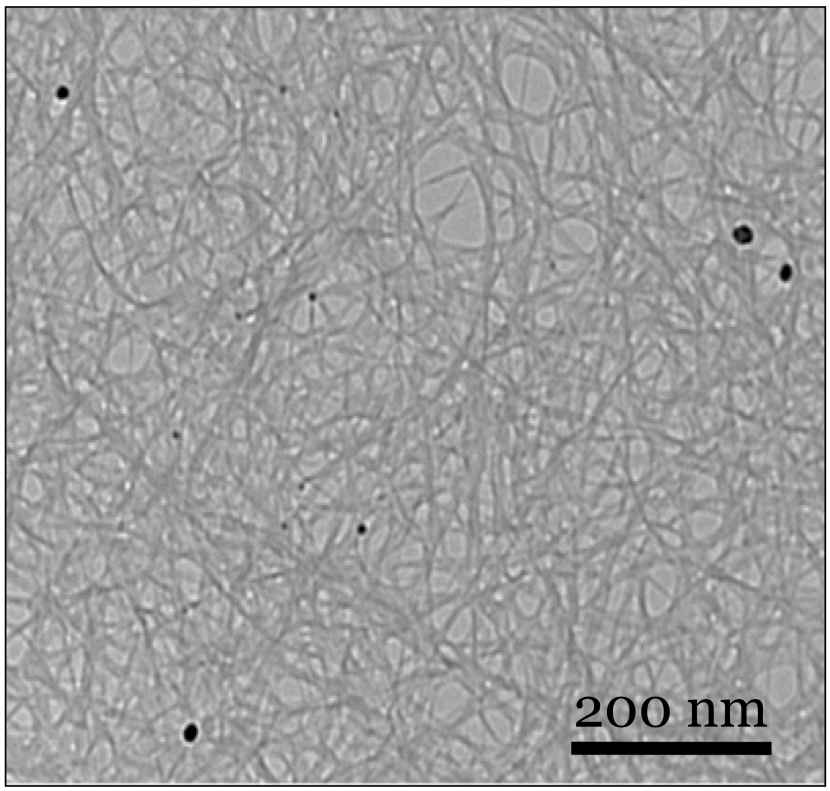

Figure 4.9 TEM image of Kevlar Nanofibers dispersed in DMSO solution. Basic DMSO environment breaks strong hydrogen bonds between Kevlar bundles and makes LBL assembly possible.

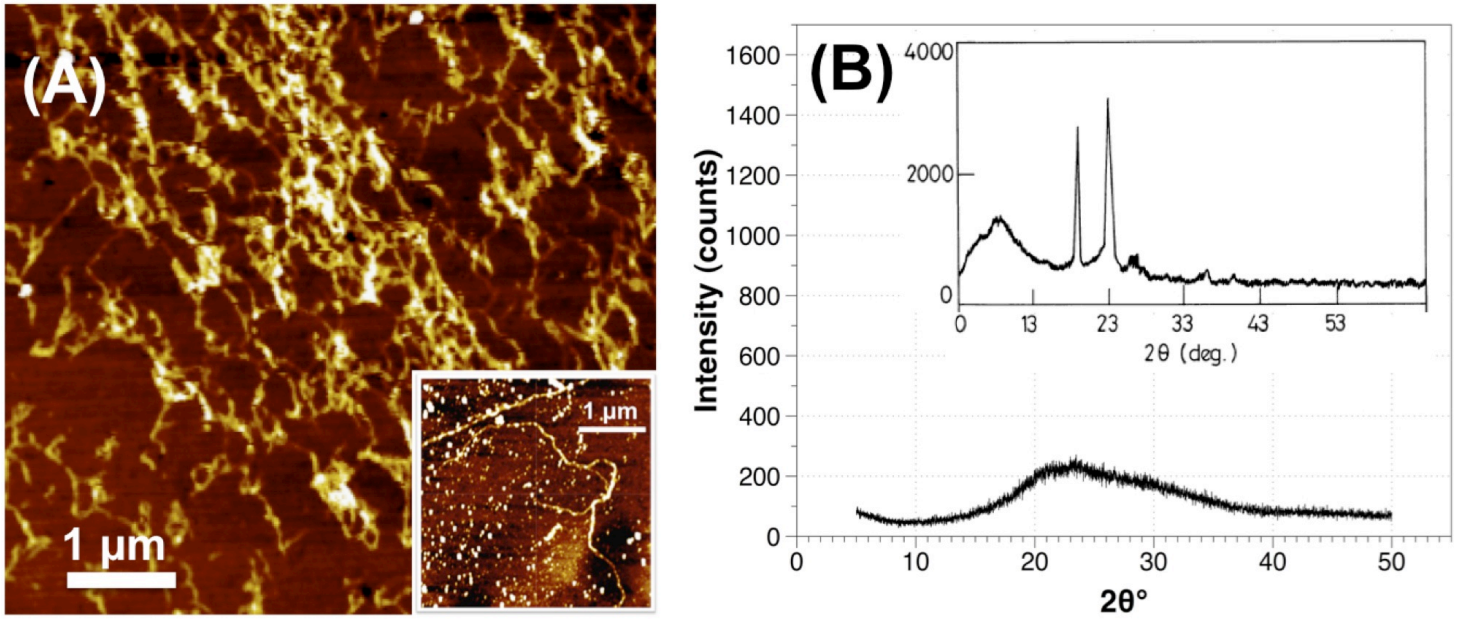

Figure 4.10 (A) AFM image of a layer of PEO-Kevlar on silicon wafer. Long kevlar as well as well defined network infrastructure can be seen very clearly. (B) XRD spectrum of LBL PEO-Kevlar membrane. No crystalline structure could be found compared to highly crystalline cast-PEO membrane (inset)

4.6.4 Scanning Electron Microscopy

Scanning electron microscopy was used to image the surface and the cross section of an as-prepared 200-bilayer PEO-Kevlar membrane. In Figure 4.11(A) we find very flat and smooth surface morphology, suggesting well-organized deposition of PEO and Kevlar even though the fabrication processes involved in both aqueous phase and organic solvent. Cross-section image shows uniform thickness across the membrane and homogeneous blending of PEO and Kevlar without common stratified structures seen in other LBL membranes (Figure 4.11(B)).

4.6.5 Mechanical Characterization – Tensile Test

Tensile test was implemented to measure the mechanical properties of the PEO-Kevlar membranes. To compare with commercial grade separator, Celgard 2400 PP separator was used. Specimens were prepared by cutting the as-prepared membranes into 1mm by 25.4 mm stripes. Due to manufacturing processes, Celgard 2400 membranes have different mechanical properties in axial and transverse direction. In Figure 4.12, one can find the behavior of Celgard 2400 membrane under tensile stress. Young's modulus, or elastic modulus, is simply the stress-strain relationship at the linear region near the start of tensile test. By linear fitting to the data, which can be found in the insets of Figure 4.6.4, one can easily estimate the Young's modulus of Celgard 2400 separator to be 1.561 GPa in axial direction and 0.3088 GPa in transverse direction. The ultimate strength of Celgard 2400 is measured to be nearly 200 MPa in axial direction and 11 MPa in transverse direction.

Figure 4.13 shows the stress-strain relation of a 100-bilayer PEO-Kevlar membrane. The ultimate tensile strength was measured to be 169 MPa. Although the ultimate strength is slightly lower than that of Celgard 2400 in axial direction, PEO-Kevlar nanocomposite has the advantage of being an isotropic material, that the mechanical strength is consistent through the whole membrane. The Young's and shear moduli are determined to be 4.95 GPa and 1.861 GPa respectively, assuming the Poisson's ration of the membrane to be 0.33. While the Young's modulus of PEO is normally around the order of 100 MPa, the data show very promising results of the reinforcement of the PEO electrolyte by Kevlar fibers.

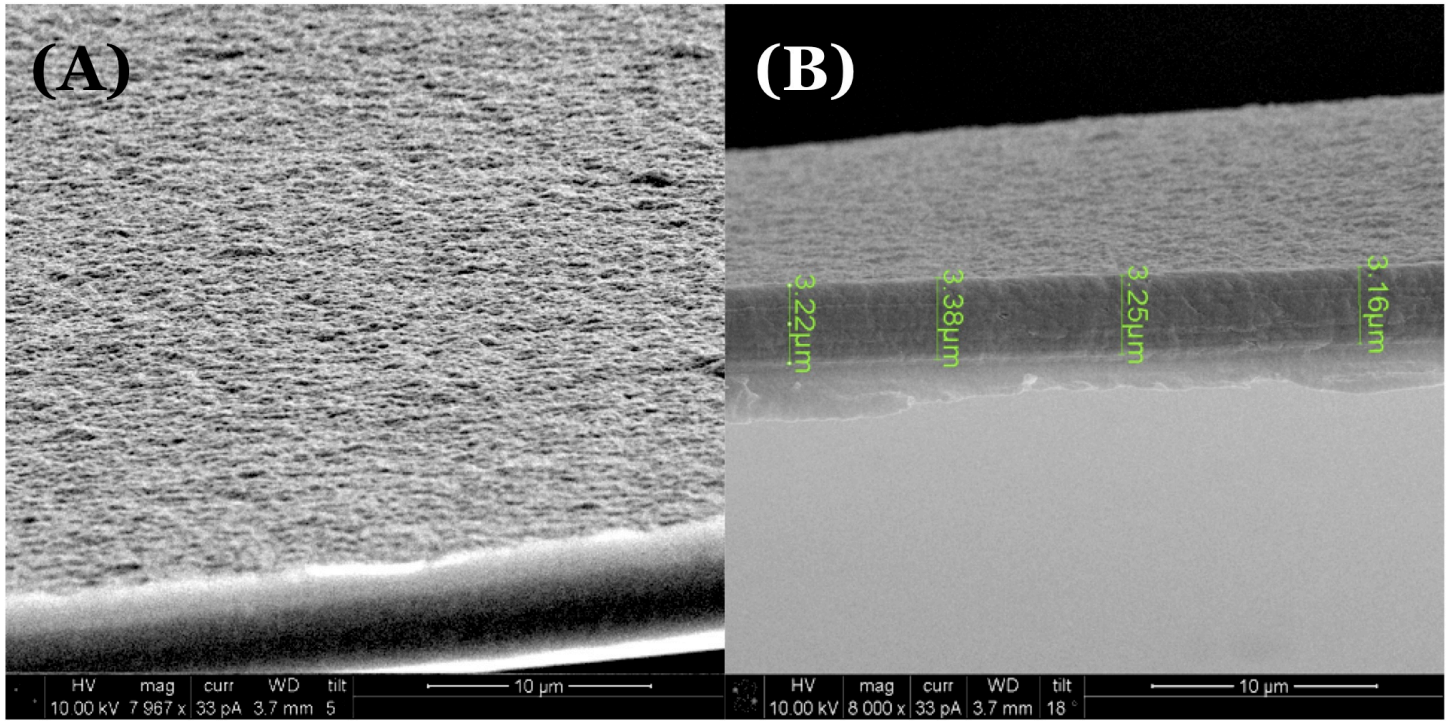

Figure 4.11 SEM images of 200-bilayer PEO-Kevlar freestanding membrane.: (A) Angled view shows uniform surface morphology; (B) Corss-section view shows highly uniform thickness across the membrane

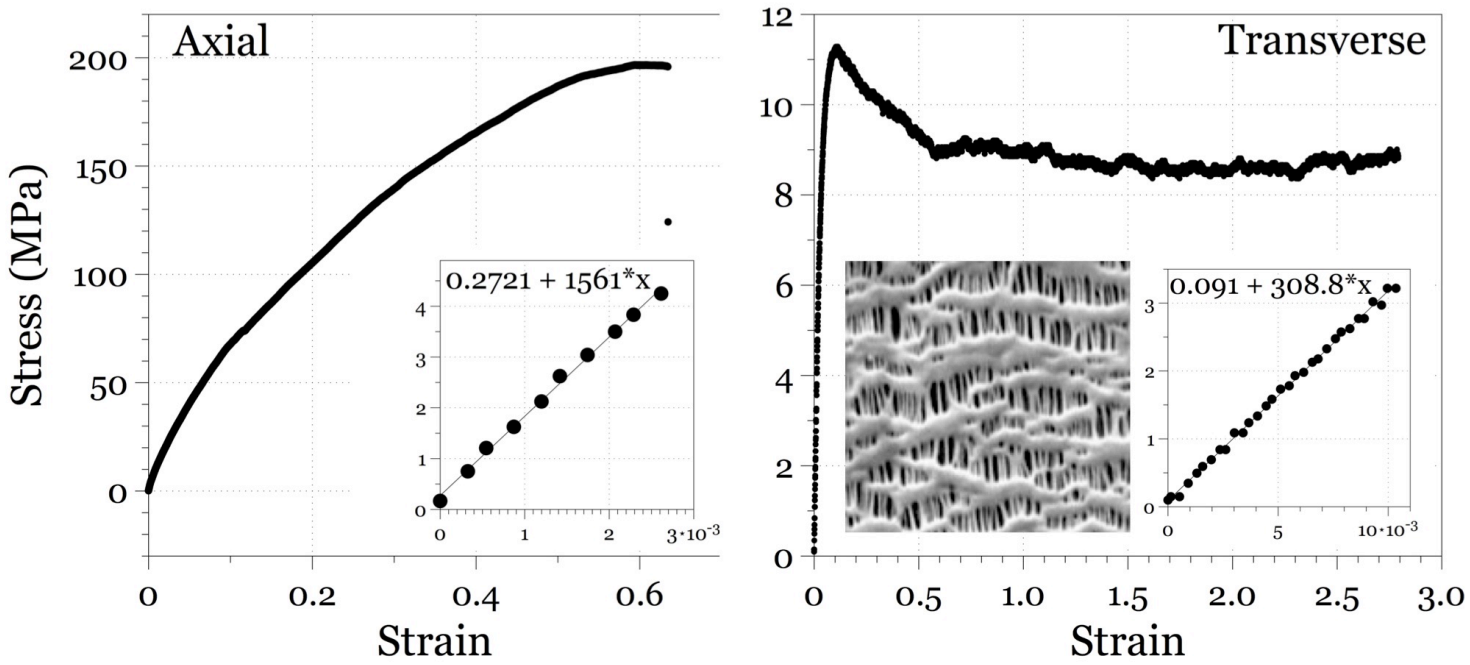

Figure 4.12 Tensile test results of Celgard 2400 commercial separator in axial (polymer chain) direction and transverse direction. Insets: linear fitting for obtaining Young's modulus of the separator.

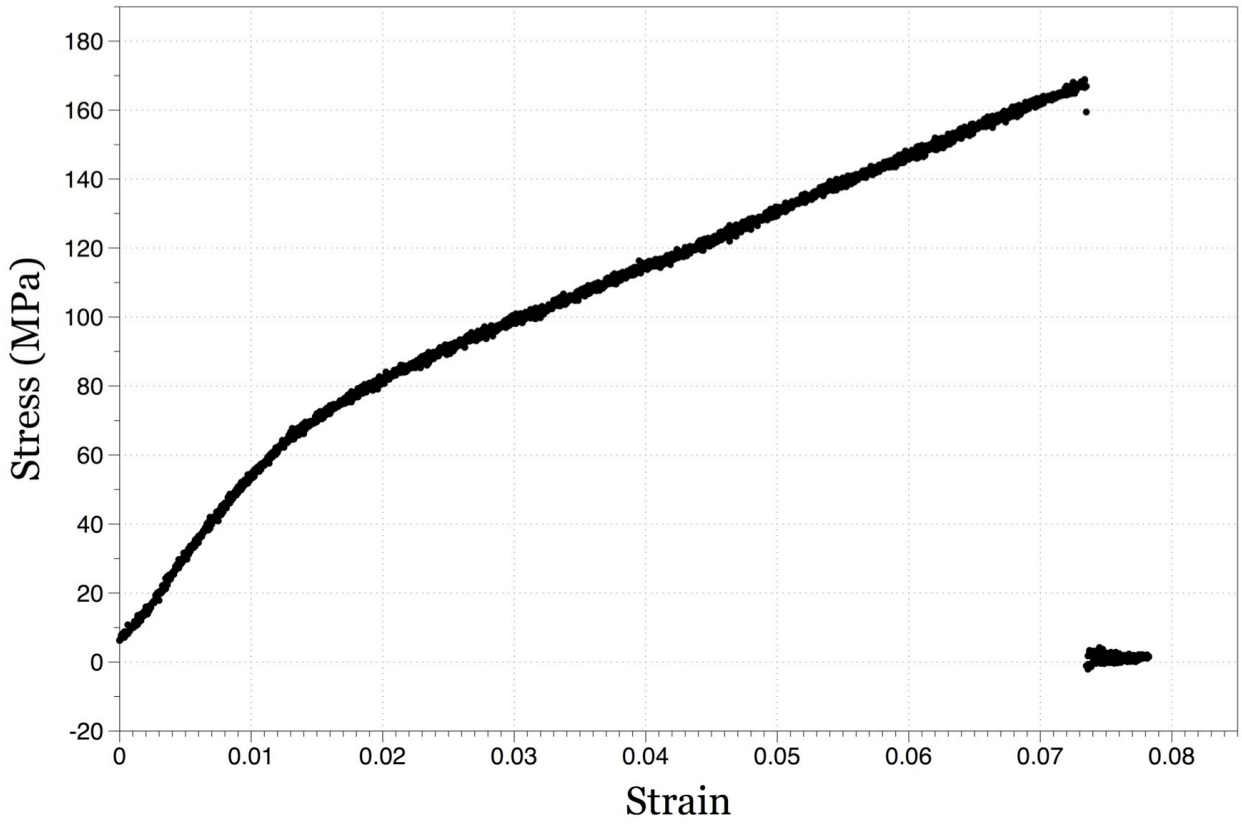

Figure 4.13 Tensile test of a 100-bilayer PEO-Kevlar membrane. Young's modulus was determined to be 4.95 GPa, while the ultimate strength is 169 MPa.

4.6.6 AC Impedance Spectroscopy

AC Impedance Analyzer (Solartron) and Potentiostat (Autolab) were used to investigate ionic conductivity of PEO-Kevlar membranes. Freestanding PEO-Kevlar films were sandwiched in between two lithium metal electrodes and housed in homemade Swagelok testing cell. Dry, as-prepared PEO-Kevlar membrane without addition of electrolyte showed lower ionic conductivity of $5.054*10^{-6}$ S/cm at room temperature. When the cell was heated up to 90 °C, the film exhibits higher conductivity at the range of $2.619x10^{-5}$ S/cm (Figure 4.14). To enhance the ionic conductivity, lithium triflate salt was incorporated into layer-by-layer assembly by adding the salt into PEO solution. PEO with 0.1 M, 0.2 M, 0.5 M, and 1 M of lithium triflate salt were prepared and incorporated into LBL membranes. However, the improvement was very limited, and as the concentration of salt went higher, the quality of the PEO-Kevlar membrane decreased. When salt concentration in PEO reached 1M, it was literally not possible to grow uniform film on top of glass substrate.

Another approach of incorporating lithium salt into the membrane was to add lithium/solvent mixture to the membrane after layer-by-layer process. Lithium salt solution was made by dissolving lithium triflate in PC (propylene carbonate) and DMC (dimethyl carbonate) mixture (PC:DMC=1:1). By adding 200 μl of 0.1 M lithium salt solution to the membrane right before loading the membrane into the testing cell, the ionic conductivity was enhanced to $2.513x10^{-5}$ S/cm. When the membrane was immersed in 1 M of lithium/PAN solution for 24 hours, given sufficient time for lithium ions to be intercalated into PEO framework, and the help from the plasticizers, the ionic

conductivity was then further improved to 5.543×10^{-5} S/cm. This puts the mechanically strong PEO-Kevlar membranes right in the working range for lithium batteries. Table 4.1 summarizes the ionic conductivities from different membrane setups.

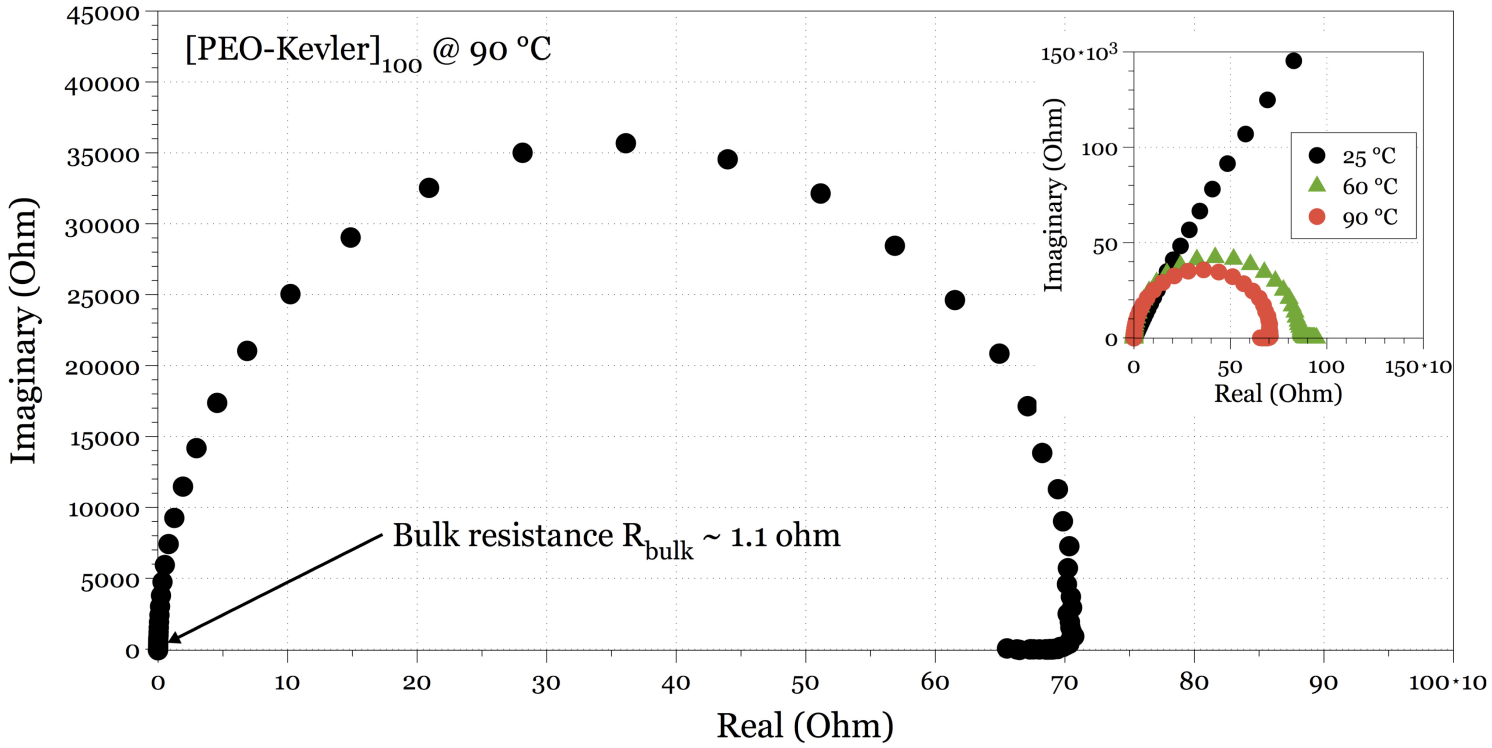

Figure 4.14 AC impedance spectroscopy of 100-bilayer PEO-Kevlar ionic conducting membrane at different temperature.

[PEO-Kevlar]	R_{bulk} (ohm)	Thickness (um)	Diameter (cm)	Ionic Conductivity (S/cm)
$[PEO\text{-}Kevlar]_{100}$ Dry @ 25°C	5.8	1.46	2.54	4.993E-06
$[PEO\text{-}Kevlar]_{100}$ Dry @ 90°C	1.1	1.46	2.54	2.619E-5
$[PEO\text{-}Kevlar]_{200}$ + Li(1M)-PC-DMC	16.2878	2.828	1.2	1.535E-05
$[PEO\text{-}Kevlar]_{350}$ + Li(1M)-PC-DMC 24hrs	16.712	9.92	1.2	**5.248E-05**
$[PEO\text{-}Kevlar]_{350}$ + Li(1M)-PC-DMC 24hrs + additional salt	15.8239	9.92	1.2	**5.543E-05**

Table 4.1 Ionic conductivity of PEO-Kevlar ICMs in different configurations.